UNIVERSITY OF CALIFORNIA, SAN DIEGO

Computational models on cell migration

A dissertation submitted in partial satisfaction of the
requirements for the degree
Doctor of Philosophy

in

Physics (Biophysics)

by

Danying Shao

Committee in charge:

Herbert Levine, Chair
Alison Coil
Terence Hwa
Bo Li
William Loomis
Wouter-Jan Rappel

2011

The dissertation of Danying Shao is approved, and it is acceptable in quality and form for publication on microfilm and electronically:

_____

_____

_____

_____

_____

_____
Chair

University of California, San Diego

2011

TABLE OF CONTENTS

LIST OF FIGURES

LIST OF TABLES

ACKNOWLEDGEMENTS

First, I would like to express my deep gratitude to my advisors Professor Herbert Levine and Dr. Wouter-Jan Rappel. Thank you for guiding me through an enlightening journey in biophysics. Your advices to my research work have always been insightful and creative. Without your help, I would not have accomplished the works concluded in this thesis.

To Professors William Loomis and Bo Li, thank you for your advices on my research. To Professor Terence Hwa, thank you for your great classes on physics and biophysics. To Professor Alison Coil, thank you for the Women in Physics meeting, which is always enlightening. I am honored to have you all serve on my thesis committee.

I would also like to thank Professor Richard Firtel, Professor Alex Groisman, Dr. Kosuke Takeda, Dr. Pascale Charest, Dr. Micha Adler for the fruitful collaboration on the Ras project.

To my lab-mates, Wen Chen, Bo Hu, Monica Skoge and Albert Bae, it's been a great pleasure working you. I am also thankful to CTBP, an excellent place for biophysics research.

To my dear husband, Minghui, thank you for your unconditional love and encouragement. Finally, I would like to thank my parents during all these years.

Chapter 2, in part, has been submitted for publication of the material as it may appear in K. Takeda, D. Shao, M. Adler, P. G. Charest, W. F. Loomis, H. Levine, A. Groisman, W. J. Rappel and R. A. Firtel, Incoherent feedforward control governs adaptation of activated Ras in a eukaryotic chemotaxis pathway. *Submitted to Science Signaling.* The dissertation author was the primary investigator and author of this paper.

Chapter 4, in part, is a reprint of the material as it appears in D. Shao, W.J. Rappel and H. Levine, Computational model for cell morphodynamics. *Phys. Rev. Lett.*, 105, pages 108104–108107. The dissertation author was the primary investigator and author of this paper.

Chapter 5, in part, is currently being prepared for submission for publication of the material, D. Shao, W.J. Rappel and H. Levine, Coupling actin flow

and adhesion mechanism during cell migration. The dissertation author was the primary investigator and author of this material.

VITA

07/2006	Bachelor of Science, Physics, Peking University
03/2008	Master of Science, Physics, University of California, San Diego
12/2011	Doctor of Philosophy, Physics (Biophysics), University of California, San Diego

PUBLICATIONS

D. Shao, W. Zheng, W. Qiu, Q. Ouyang and C. Tang. Dynamic Studies of Scaffold-Dependent Mating Pathway in Yeast. *Biophys. J.*, 91(11), pages 3986–4001.

D. Shao, W.J. Rappel and H. Levine. Computational model for cell morphodynamics. *Phys. Rev. Lett.*, 105, pages 108104–108107.

K. Takeda, D. Shao, M. Adler, P. G. Charest, W. F. Loomis, H. Levine, A. Groisman, W. J. Rappel and R. A. Firtel. Incoherent feedforward control governs adaptation of activated Ras in a eukaryotic chemotaxis pathway. *Submitted to Science Signaling.*

D. Shao, W.J. Rappel and H. Levine. Coupling actin flow and adhesion mechanism during cell migration. *In preparation.*

ABSTRACT OF THE DISSERTATION

Computational models on cell migration

by

Danying Shao

Doctor of Philosophy in Physics (Biophysics)

University of California, San Diego, 2011

Herbert Levine, Chair

Cell migration is one of the most intriguing areas in cell biology and has attracted many interdisciplinary studies. It is regulated by complex biochemical signaling networks and comprises many mechanical processes, including protrusion, adhesion, translocation of the cell body and retraction of the rear.

This dissertation starts with the signaling pathway that senses external chemoattractant, specifically, the Ras pathway (Chapter 2). We found that the response of an activated Ras shows near perfect adaptation. We attempted to fit the results using mathematical models for the two possible simple network topologies that can provide perfect adaptation. Only one, the incoherent feedforward network, is able to accurately describe the experimental results. This analysis re-

vealed that adaptation in this Ras pathway is achieved through the proportional activation of upstream components and not through negative feedback loops.

From Chapter 3 to Chapter 5, we integrated chemical reactions inside the cell with the mechanical process of cell migration. In Chapter 3, we set up a framework, based on phase field method, to describe the cell shape and the chemical reactions in a moving cell. Under this framework, we developed a computational model on cell morphodynamics in Chapter 4. Our model incorporates the membrane bending force and the surface tension and enforces a constant area. Furthermore, it implements a cross linked actin filament field and an actin bundle field that are responsible for the protrusion and retraction forces, respectively. The model was successfully applied to fish keratocytes and *Dictystelium* cells.

In Chapter 5, we studied the coupling between adhesion mechanism and actin flow in keratocytes. The adhesion mechanism incorporated both the gripping mode and the slipping mode. The model-predicted maps of actin flow, substrate stress and the alignment between the two are quantitatively consistent with experimental observations. Furthermore, we explored the phase diagram of cell migration by varying myosin II and adhesion strength. Our model suggested that the pattern of the actin flow inside the cell, the cell velocity and the cell shape are determined by the integration of actin polymerization, myosin contraction, the adhesion and membrane forces.

Chapter 1

Introduction

The science of cell biology has evolved dramatically during the last decades. With the development in technology, biologists are no longer satisfied with qualitative data, but strive for innovative quantitative experiment. Meanwhile, many researchers from other fields, including physics, mathematics and computational science, have been lured by the complexity of biological systems. They bring in various analysis methods, modeling and simulation techniques, and more importantly, different perspectives. The interdisciplinary research has produced fruitful results and revealed many underlying mechanisms of biological systems.

Cell migration refers to the translocation of cells. It is one of the most intriguing areas in cell biology and has attracted many interdisciplinary studies. It is a fundamental process in many biological systems, for example, the development of embryos, wound healing and the inflammatory response. Inappropriate migration may cause severe diseases, such as immunosuppresion, defective wound repair, or tumor dissemination [64, 72]. The studies on cell migration may focus on different levels. The complexity of cell migration fosters multi-scale studies, from molecular scale, to whole cell scale, and up to the colony scale. I focus on the cell scale.

1.1 Signaling pathways

During migration, the cell presents a front-rear polarity. Molecules with distinct functions have different distributions between the front and the back. De-

pending on the cell type, some cells, such as Keratocytes, can polarize spontaneously in the absence of external cues. In other cells, polarity may be dictated by the extracellular environment. For example, the *Dictyostelium* cells are able to sense gradients of chemoattractants (the extracellular chemical signals) and move towards their source. This process is called chemotaxis, which is regulated by signal transduction pathways that senses and amplifies the gradient of external chemoattractant [43].

Chapter 2 studies the Ras signaling pathway. It has been found that Ras plays an essential role in regulating *Dictyostelium* chemotaxis, but the mechanisms that regulate Ras activity during chemotaxis are not well understood [15]. We used a microfluidic device to observe the dynamics of Ras activity. Following a change in external input, Ras goes through a transient response and returns to a fixed base-level, a phenomenon called adaptation. Adaptation in signaling systems often involves negative feedback loops and plays a crucial role in eukaryotic chemotaxis. We determined the dynamical response of a eukaryotic chemotaxis pathway immediately downstream from G protein-coupled receptors following a uniform change in chemoattractant concentration. We found that the response of an activated Ras shows near perfect adaptation. We attempted to fit the results using mathematical models for the two possible simple network topologies that can provide perfect adaptation. Only one, the incoherent feedforward network, is able to accurately describe the experimental results. This analysis revealed that adaptation in this Ras pathway is achieved through the proportional activation of upstream components and not through negative feedback loops. Furthermore, these results are consistent with a local excitation/global inhibition mechanism for gradient sensing, possibly with a RasGAP as a global inhibitor.

Multiple signaling pathways are initiated and organized at the cell surface. They intertwine with each other and form a signaling network, which is tightly regulated during cell migration. The signaling networks coordinate various mechanical events, including cell protrusion, adhesion, translocation of the cell body and retraction of the rear [10].

1.2 Mechanical events during cell migration

Previous studies have identified several molecular components in each event and many mathematical models have been proposed to explain a specific event. For example, cell protrusion is powered by actin polymerization. The actin filament (F-actin) is a polar structure with a barbed end pointing towards the cell membrane. It polymerizes by adding ATP-bound monomers to the barbed end, generating a protrusion force.

The mathematical models for actin polymerization generally falls into three categories: 1) the barbed ends are persistently attached to the cell membrane; 2) the barbed ends fluctuate freely; or 3) some barbed ends are attached while others are free. The model predicted relationship between the force generated by actin protrusion and the elongation rate was then compared with the experimental data [23].

Another interesting question concerns how the cell pulls up its rear (the retraction event). In keratocytes, it is believed that myosin II collapses the actin network and transforms it to parallel bundles [65]. In addition, cell adhesion, the interaction between cells or between cell and extracellular matrix (ECM), also attracts intensive studies [35]. Various models have been proposed for the force generation and turnover dynamics of adhesion sites [10, 13, 17].

1.3 Integrated modeling on cell migration

Cell migration is governed by various biochemical and mechanical events. The speed of cell motion and the deformation of cells during migration are determined by the interaction of all those events. Despite the current knowledge of each event, how the events are coordinated and combined is poorly understood.

1.3.1 Literature review

Cell migration has attracted many modeling efforts. There are several 2D Monte Carlo Models. In the minimal model [83], Satyanarayana and Baumgaertner

treated the polymerizing and depolymerizing of the actin filaments as a stochastic process. Here, F-actin was immobile, assumably due to the strong adhesion, representing the necessary force to break the symmetry and push the cell forward. The cell membrane was represented by a flexible non-self-avoiding ring that went through random walk. They predicted a optimal value of the fraction of F-actin for cell speed. Maree *et al.* also constructed a 2D stochastic model where the protrusion rate was dependent on the density of the barbed end [59]. Their model further incorporated the dynamics of Cdc42, Rac and Rho. A similar model was advanced in Satulovsky *et al* [82]. In this paper, focal adhesion sites formed stochastically at protrusive perimeter points and disassembled stochastically. Note that focal adhesions were modeled as point constraints of cell retraction and retraction was inhibited when a perimeter point hit a focal adhesion. These models were generally based on phenomenal rules. Although they were able to give shapes that assembled real cells, these models lacked a solid interpretation of the underlying physical processes.

Another category of efforts is to write down the various forces involved during cell migration, translate these forces into local velocity, and then evolve the cell shape conformably using level set method or phase field method. For example, Yang *et al.* used level set to model the cellular deformation[104]. They considered the protrusion pressure, retraction pressure, volume penalty and tension force, and the total pressure was written as

$$P_{total} = P_{pro} + P_{ret} + P_{vol} + P_{ten}.$$

The membrane velocity was determined by the dashpot-spring model. Specifically, the viscous cytoplasm was modeled as dashpot, and the viscoelastic cytoskeleton which connected cytoplasm to the membrane was modeled as paralleled springs. These two parts were then linked in series. Note that the velocity was only defined on the membrane, and was extended to other places by nearest neighbor method. The cell membrane were updated according to the equation

$$\frac{\partial \phi}{\partial t} + v \cdot \nabla \phi = 0,$$

where ϕ is the level set field, v is the local velocity. To keep the profile of the

interface, that is to prevent the interface from becoming steep or flat, the level set potential has to be re-initialized at each iteration

$$\frac{\partial \phi}{\partial t} = S(|\nabla \phi| - 1),$$

where $S = 1$ indicates the inside of the cell and $S = -1$ the outside of the cell. However, they failed to get the right cell deformation with constant pressure. Instead, they simulated backwards, form cell morphologies to get the time-course of the pressure. In addition, in their model, the PIP_3, which controlled protrusion and retraction strengths, was simply proportional to external cAMP level.

Misbah's group have used phase field method to simulate vesicles' deformation and tumbling [9, 8]. They used fluid dynamics to calculate the velocity field

$$\epsilon \frac{\partial v}{\partial t} = \nabla \cdot \sigma - \nabla p + F_c + F_\zeta,$$

where $\sigma = \eta(\phi)[\nabla v + (\nabla v)^T]$, p is the pressure, F_c is the curvature tern, F_ζ conserves local mass. And the phase field ϕ is determined by

$$\frac{\partial \phi}{\partial t} = -v \cdot \nabla \phi + \Gamma(\nabla^2 \phi - \frac{1}{4\epsilon^2} g'(\phi) + c|\nabla \phi|)$$

The second term here is to restrict the profile of the interface automatically. Note that they modeled vesicles as incompressible fluid $\nabla \cdot v = 0$. Although reasonable for rigid vesicles, this assumption may not be valid for cells.

Du's group also employed phase field method to study the three-dimensional deformation of a vesicle membrane, but in an different approach [24]. They developed an energetic variational formulation to give an effective Eulerian description. Under the elastic bending energy, with prescribed bulk volume and surface area, they studied both the static and the dynamic deformations. Lowengrub *et al.* extended the model and studied the multi-component vesicles [56]. To describe two different components of the vesicle membrane, they added another layer of phase field. They successfully simulated the processes of spinodal decomposition, coarsening, budding, and fission. Du's group recently started taking account of the substrate adhesion [107]. Most of these phase field models were applied to vesicles and could not be used to model cell migration directly. Several important

factors that were not present in vesicle models include, to name a few, the chemical reactions and the mechanical properties of actin network.

With the improvement of imaging technology, the actin flow was observed and quantitative velocity field was mapped. Mathematicians started to model this interesting phenomenon. Larripa and Mogilner suggested a one dimensional actin flow gel model [51]. The actin network was described by Kelvin-Voight model – a spring in parallel with a dashpot. The gel's deformation was calculated by displacement $u(x,t) = x'(x,t) - x_0$, where x is the coordinate of the unperturbed material point. Then

$$\beta \frac{\partial u}{\partial t} = h \frac{\partial \sigma}{\partial x}$$

The left hand side was the viscous drag force from adhesion, while the right hand side described various stresses, including elastic, viscous and bundle stresses

$$\sigma = E \frac{\partial u}{\partial x} + \mu \frac{\partial^2 u}{\partial x \partial t} + T.$$

The strength of the stresses was related to the F-actin density and the actin-bound myosin density, which were modeled by a set of chemical reaction equations.

Their model predicted that the front half of the cell had a graded retrograde flow of actin network. However, the maximum speed at leading edge was approximate equal to the cell speed, which contradicted the experiment result that retrograde flow was less than 1/10 of cell speed. Some of their model assumptions were questionable. First of all, the gel's deformation equation requires that elastic strain be small compared to unity. During the cell migration, the actin network continuously deforms and the displacement u(x,t) could be rather large. Thus, the above assumption is unlikely to be true during cell migration. Actually, Mogilner's group turned to viscoelastic fluid models in the later works (see below). Secondly, in the model, the cell's forward movement resulted from the actin assembly rate v_p and depolymerization rate v_d. However, both v_p and v_d were hand woven and not generated from the physical forces. This brings up the question of momentum conservation during the cell migration. Aside from the centripetal actin flow, the model did not answer the deep question–how the adhesion coupled actomyosin machine drives the cell forward. Besides, the asymmetric distribution of actin and

myosin in the model was enforced by the arbitrary boundary conditions and the adhesion was simplified as a viscous drag.

In the two dimensional viscoelastic flow model presented in [79], both the cell geometry and the cell speed were prescribed stationary and outside the model. The velocity of actin network in the lab frame u followed

$$\rho\frac{\partial u}{\partial t} = \nabla \cdot [(1-\alpha)\eta(\nabla u + (\nabla u)^T) + \tau] + \nabla \cdot \tau^{myo} + F_{adh}$$

where the the stress tensile followed Maxwell model

$$\tau + \lambda(\frac{\partial \tau}{\partial t} + u \cdot \nabla \tau - \tau \cdot \nabla u - (\nabla u)^T \cdot \tau) = \alpha\eta(\nabla u + (\nabla u)^T).$$

Note that when $\lambda = 0$, it would come back to Navier-Stokes equation which applies to newtonian fluid. The graded F-actin density was again forced by boundary conditions. And myosin was modeled in two states: one was bounded to the F-actin, and the other was free. Myosin could transfer between the two states and only the bound myosin could generate the contractile stress. They also prescribed a nonuniform adhesion strength field, which was larger along the leading edge and at the sides, in order to mimic the real cell condition.

In the later models [3, 99], the cell shape became an output produced from the model. The boundary velocity was a function of the protrusion rate and the actin flow velocity. However, the protrusion rate was again modeled in a phenomenal fashion. The work in [3] investigated the effects of different adhesion strength to the cell shape. Note the adhesion in their model was purely frictional. In the paper [99], they suggested four different minimal mechanisms for cell migration: 1) myosin contraction-driven motility; 2) G-actin transport-limited motility model; 3)Rac/Rho-regulated motility; and 4)microtubule-based transport of vesicles to the leading edge limits the rate of protrusion. They suggested that these models, alone or in combination, might serve to drive the cell forward.

The above models included the cell membrane and the cytoskeleton that hosted F-actin. A more complicated model also took account of the cytsol [22, 41]. It is sometimes called Reaction Interpenetrative Flow (RIF) model. In this model, the cell membrane serves as the boundary to control flux and conduct stress. The cytoskeleton, the same as before, is viscoelastic and generates active force through

myosin. The cytosol is modeled as flow and may convert to the cytoskeleton through the polymerization/depolymerization process

$$G - actin \rightleftharpoons F - actin.$$

Let $v_{n,s,m}$ be the velocity of actin network/solution/membrane, and $\theta_{n,s}$ the volume fraction of network/solution and $\theta_n + \theta_s = 1$ (according to mass conservation). The interchange between cytoskeleton and cytosol can be written as

$$\begin{aligned} \frac{\partial \theta_n}{\partial t} &= -\nabla \cdot (\theta_n v_n) + J \\ \frac{\partial \theta_s}{\partial t} &= -\nabla \cdot (\theta_s v_s) - J \\ \nabla \cdot (\theta_n v_n + \theta_s v_s) &= 0 \end{aligned}$$

Here, J is the exchange rate between network and solution.

Mechanically, the Cytosol feels the viscous friction from the cytoskeleton and the pressure shared with cytoskeleton, and follows Darcy's law. As for the cytoskeleton, in order to simplify the viscoelastic model, the elastic property was separated from the viscous property.

However, the contribution from the extra complexity was limited according to simple estimates. For example, the actin flow rate, ranging from zero to about $0.1\mu m/s$, divided by the hydraulic permeability of the cytoskeleton, 0.01 $\mu m^3/(pN \cdot s)$, gives the respective stress of about 10 $pN/\mu m^2$. This is much smaller than the myosin contractile stress in keratocyte, which is about 100 $pN/\mu m^2$. Also, the Deborah number $De = \lambda V/L \sim 1s \times 0.5\mu m s^{-1}/10\mu m \sim 0.05$ is small, so the system is effectively viscous [79].

The work by Carlsson gave an analytic result of cell motion in one dimension [12]. The most interesting point in this paper is that he treated the actin protrusion as an active stress, similar to the myosin contractile stress, although in the opposite sign. It provided us a uniform way to model the actin protrusion and myosin contraction on a solid physics ground and avoid using a phenomenal protrusion rate as described above.

In addition, some models were extended from the actin polymerization models (see above), and thus more focused on the actin dynamics in the leading edge. For example, the model in [111] separated the actin network into two regions: the actomyosin gel which consists of cross-linked actin filaments, and the semiflexible region at the leading edge. The velocity of the lamellipodium was then determined by the interactions between the actomyosin gel, the semiflexible region and the adhesion. These models do not solve cell shapes.

1.3.2 Summary of my works on cell migration modeling

We aim to create a computational framework, based on phase field method, that integrates all the essential events during cell migration. By comparing the outputs, such as cell speed, cell shape, actin flow map and stress map, with experiments, we'll be able to verify the current understanding of individual processes and reveal potential couplings between different events.

It presents us a great computational challenge since it is a moving boundary problem. We use phase field method because it is both efficient and relatively easy to implement. Phase field method has been previously applied to solidification [75], crack propagation [47], viscous fingering [30] and diffusional problems in complicated geometries [28, 49]. In cell biology, it's been used to simulate the deformation of membranes [9, 8, 24] and the chemical reactions in a stationary cell [49]. In Chapter 3, I introduced the setup of the phase field method and applied it to a simple case - vesicles with fixed volume and area. I also extended the method to describe the chemical reactions in a moving cell. This chapter is a preparation for Chapter 4 and Chapter 5.

In Chapter 4, we developed a computational model for cell morphodynamics. Our model incorporates the membrane bending force and the surface tension and enforces a constant area. Furthermore, it implements a cross linked actin filament field and an actin bundle field that are responsible for the protrusion and retraction forces, respectively. We first applied it to fish keratocytes. The model predicts steady state cell shapes with a wide range of aspect ratios, depending on system parameters. Moreover, we find that the dependence of the cell speed on this

aspect ratio matches experimentally observed data. We then applied the model to *Dictyostelium* cells and simulated the crawling process guided by patches.

In Chapter 5, we studied the coupling between adhesion mechanism and actin flow. The adhesion mechanism incorporated both the gripping mode and the slipping mode. The model-predicted maps of actin flow, substrate stress and the alignment between the two are quantitatively consistent with experimental observations. Furthermore, we explored the phase diagram of cell migration by varying myosin II and adhesion strength. Our model suggested that the pattern of the actin flow inside the cell, the cell velocity and the cell shape are determined by the integration of actin polymerization, myosin contraction, the adhesion and membrane forces.

Chapter 2

Incoherent feedforward control governs adaptation of activated Ras in a eukaryotic chemotaxis pathway

2.1 Introduction

Many biological systems that exhibit perfect adaptation employ an integral control strategy in which a buffering component of the signaling network integrates the difference between the response and desired basal level. This difference is then fed back to achieve perfect adaptation through negative regulation. Examples include: bacterial chemotaxis [2, 6, 26, 106], yeast osmo-regulation [67], and calcium homeostasis in mammals [25]. Integral control, however, is not the only way to accomplish perfect adaptation. A systematic computational analysis of a three-node network revealed that a second network topology can achieve robust perfect adaptation [4, 58]. This topology employs an incoherent feedforward mechanism [87] in which two nodes of the network are activated proportionally by the input stimulus. These two nodes then act on the third node with opposite effects (i.e., one activates and one inhibits), leading to a transient response that adapts per-

fectly. To date, no clear examples of biological networks that use the incoherent feedforward strategy have been identified. This is perhaps surprising since it can be shown that networks that contain incoherent feedforward loops perform better than networks that employ integral control [58]. Eukaryotic cells can respond to steep or shallow chemoattractant gradients over a wide range of chemoattractant concentrations [32, 89]. Not surprisingly, it has been suggested that adaptation is a key component of eukaryotic chemotaxis and is essential for gradient sensing [54, 62, 70, 108]. Indeed, many downstream biochemical components involved in the chemotaxis pathways display adaptive behavior [94, 102, 110]. The precise mechanism of this adaptation, however, is not clear although it has been shown that it occurs downstream from the chemoattractant receptor s and coupled heterotrimeric G proteins [43]. Furthermore, even though many components of the chemotactic pathways have been described, the precise mechanisms of gradient sensing are not fully understood. A number of models for the initial response to gradients have been proposed, most of which contain a global inhibitor that provides communication between the different parts of the cell [7, 54, 55, 73, 77, 70]. It remains a challenge to distinguish between the different proposed mechanisms in the absence of quantitative data for the kinetics of the underlying pathways.

2.2 Experimental results

To measure the adaptation kinetics of a eukaryotic chemotaxis signaling pathway, we exposed cells of the social amoeba Dictyostelium discoideum to sudden uniform (global) increases and decreases in the concentration of the chemoattractant cAMP using a microfluidic device (Figure 2.1A) and examined the dynamics of activated Ras, Ras-GTP. For this, we used the Ras binding domain of human Raf1 (RBD-GFP) as a reporter, which preferentially measures activated RasG, the upstream activator of PI3K [46, 80, 108]. Ras proteins are molecular switches that bind to and activate downstream effectors when in their activated GTP- but not GDP-bound state, with different Ras proteins activating a range of effectors. Ras proteins are activated by RasGEFs (guanine nucleotide exchange factors),

which exchange Ras-bound GDP for GTP, and are inactivated by a slow, intrinsic GTPase activity which can be stimulated > 103 fold by RasGAPs (GTPase activating proteins). In unstimulated cells, RasG-GDP is distributed uniformly along the plasma membrane. Following the sudden exposure to a chemotactic gradient, RasG is rapidly and locally activated within seconds at the front of the cell [80]. This is followed by the Ras-GTP-dependent activation of PI3K and the translocation of PI(3,4,5)P3-binding PH domains to the sites of RasG activation [33, 60, 69, 80]. Activation of RasG, and a second Ras, RasC, at the leading edge is the earliest measurable signaling event in a sequence of spatially-localized cellular redistributions of signaling molecules that eventually lead to chemotactic motility [14, 76, 80, 90].

Using a microfluidic device, we switched the chemoattractant concentration in the medium surrounding the cells within <1 second (Figure 2.1B). Multiple cells were imaged every 0.63 s using spinning disk confocal microscopy and the dynamics of activated Ras was followed by the translocation of RBD-GFP to the cell cortex (Figure 2.1C). We quantified the dynamics of Ras-GTP by selecting a cytosolic region of interest and measured the RBD-GFP intensity as a function of time. Figure 2.1D shows a typical time course of the cytosolic fluorescence intensity, I(t), normalized by the average cytosolic intensity before cAMP stimulation and corrected for bleaching (see material and methods). Prior to a change in the chemoattractant concentration, RBD-GFP is uniformly distributed in the cytosol, with a low, basal level at the plasma membrane. Following an increase in chemoattractant, RBD-GFP translocalizes rapidly to the cell membrane by binding Ras-GTP, reaching a maximum at ~ 3 s. This is followed by a more gradual return to the cytosol where the RBD-GFP intensity returns to its basal level in <35 s. We have verified that the intensity of membrane-associated RBD-GFP is inversely related to cytosolic RBD-GFP fluorescence, further illustrating the translocation of RBD-GFP from cytosol to the membrane and back (Figure 2.2).

We quantified the degree of adaptation of Ras-GTP by exposing previously unstimulated cells to different chemoattractant concentrations, ranging from 1.0×10^{-2} to 1.0×10^{3} nM. The results for the 5 highest concentrations are shown in

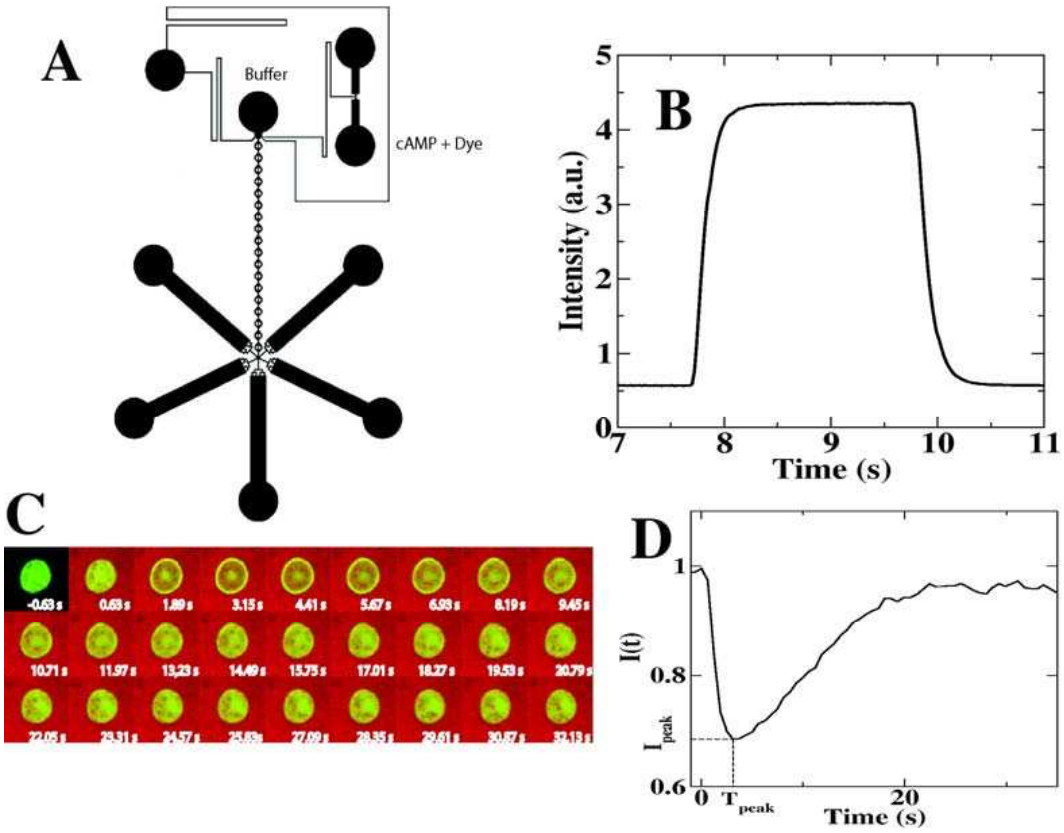

Figure 2.1: Sudden change in uniform chemoattractant results in a transient response of RBD-GFP to the membrane. (A) Drawing of channels of the microfluidic device employed in our experiments. (B) The concentration in a test chamber of the device is switched within 1 sec, as demonstrated by recording the fluorescence intensity of a dye. (C) Images of a Dictyostelium cell undergoing a sudden increase in cAMP concentration at t=0 sec. (D) The cytosolic fluorescence intensity of RBD-GFP, normalized by the fluorescent intensity before stimulation and corrected for bleaching, as a function of time following a sudden 1 μM cAMP increase at t=0 sec. The amplitude of the maximum response, I_{peak}, and its time point, T_{peak}, are recorded for each experiment.

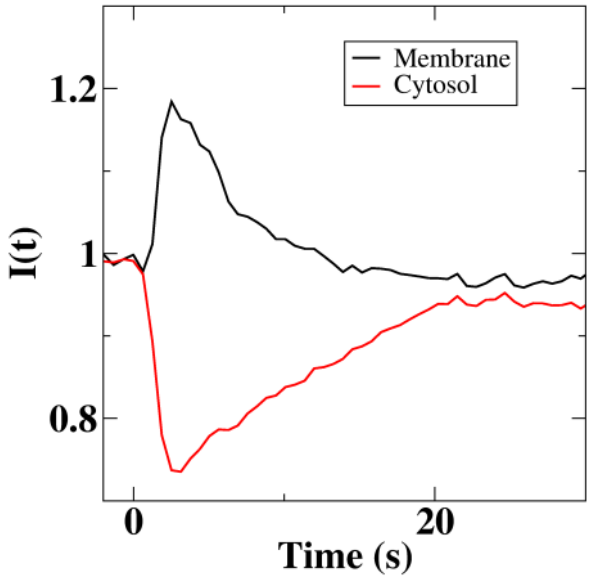

Figure 2.2: The cytosolic (red line) and the membrane fluorescence intensity following a sudden increase in chemoattractant concentration at t=0 sec.

Figure 2.3A and represent the average response of n=60 cells from three different experiments. The response increases for increasing concentrations and saturates by 1 μM. Furthermore, the peak time, T_{peak}, defined as the time from the addition of the stimulus to the peak of the response, decreases with increasing concentration, consistent with previous experiments on the kinetics of PIP3, a signaling component downstream from activated Ras [101]. As shown (Figure 2.3B), by 35 s, the normalized RBD-GFP level has returned to the pre-stimulus level for all chemoattractant concentrations, indicating that Ras-GTP adaptation is near perfect over a wide range of stimuli.

To further quantify the adaptation kinetics of Ras-GTP, we exposed cells to a constant chemoattractant concentration for 10 min, followed by a sudden increase in chemoattractant concentration. We computed the response (maximum decrease in cytosolic RBD-GFP fluoresence), I_{peak}, which reflects the translocation of the reporter to the membrane. These values were normalized by the maximum response in naive (not pre-treated) cells following a 1 μM stimulus. The results are shown in Figure 2.3C for four different levels of pre-stimulation (0, 1, 10 and

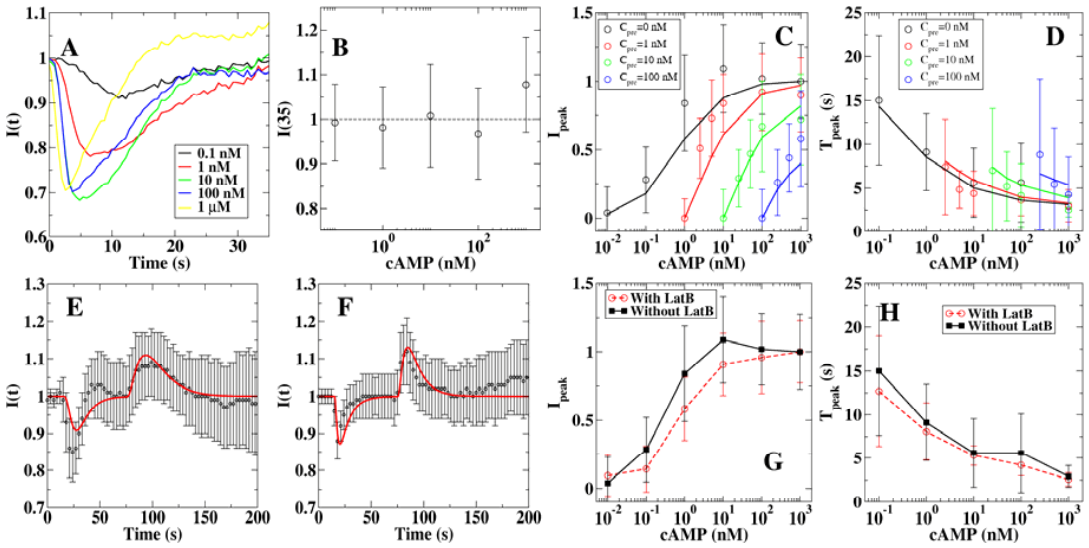

Figure 2.3: Ras response adapts over a large range of concentrations. (A) The RBD-GFP cytosolic fluorescence intensity I(t) as a function of time for different levels of stimulation. (B) The cytosolic fluorescence intensity of RBD-GFP after 35 s as a function of the cAMP concentration. (C) The RBD-GFP dose-response curves for different pre-treatment concentrations. The symbols are the experimental results while the solid lines are the results of our numerical simulations using the incoherent feedforward network. The error bars here, and elsewhere in this paper, represent the standard deviation. (D) The time of the maximum RBD-GFP response for different pre-stimulation and stimulation levels of cAMP (experiments: symbols, simulations: solid lines). (E) and (F), I(t) as a function of time following a sudden increase (at 15 s) and a sudden decrease (at 75 s) of cAMP concentration. The symbols correspond to the experimental results while the solid lines represent our numerical results. In E, the concentration increased from 0 to 0.2 nM, then decreased back to 0 nM. In F, cells were exposed to 100 nM, followed by a sudden increase to 1 μM and a subsequent drop back to 100 nM. (G) The dose response curve for untreated cells following a sudden increase of cAMP with (red) and without latrunculin B (black). (H) The peak time of the response as a function of cAMP concentration with (red line) and without latrunculin B (black line).

100 nM). Cells that were not pre-treated with cAMP were able to respond to a chemoattractant increase that spanned 3-4 orders of magnitude with an EC50 of approximately 0.25 nM. Furthermore, even cells that were pre-treated with 100 nM showed a significant response to a sudden increase in stimulus. Figure 2.3D shows T_{peak}, which, for the four different pre-stimulus levels, decreases for increasing chemoattractant.

Finally, we also examined the Ras-GTP kinetics in cells that were exposed to a sudden increase and a subsequent sudden decrease in cAMP. The results for two of these experiments are shown in Figure 2.3E and F. In Figure 2.3E, the concentration went from 0 nM to 0.2 nM and back to 0 nM. As before, the cytosolic RBD-GFP fluorescence decreased (due to translocation of the reporter to the cortex) following the increase in chemoattractant, while the decrease in cAMP concentration led to a rapid increase in the cytosolic RBD-GFP fluorescence and a subsequent slow return to the basal level. Figure 2.3F shows the results of a similar experiment where the concentrations changed from 100 nM to 1000 nM and back to 100 nM. Compared to the experiment in Figure 2.3E, the return to basal level after the decrease in cAMP concentration is markedly faster.

Previous studies identified a number of feedback loops that involve activated RasG, PI3K, and F-actin polymerization [15, 29, 71, 80, 81]. To determine the role of the F-actin feedback loop in the observed adaptation, we treated cells with 15 μM latrunculin B to block F-actin polymerization. Again, we found that the cytosolic RBD-GFP levels return to basal levels following a sudden change in chemoattractant concentration, indicating adaptation was not affected (Figure 2.4). Furthermore, latrunculin B treatment does not have a significant effect upon either the dose response curve (Figure 2.3G) or the characteristic response time (Figure 2.3H). These results show that RasG adaptation does not involve feedback loops containing actin and that the signaling network responsible for the observed perfect adaptation is upstream from F-actin polymerization.

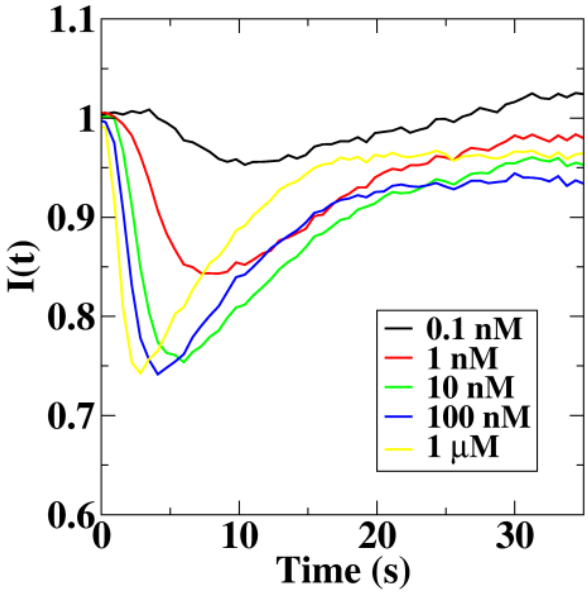

Figure 2.4: The RBD-GFP cytosolic fluorescence intensity I(t) as a function of time for different levels of stimulation in cells treated with latrunculin B.

2.3 Mathematical models on Ras pathway

This finding, combined with previous experimental results that demonstrate that adaptation occurs downstream from the receptors [43], motivated us to construct a mathematical model for adaptation that only contained Ras-GTP, RasGEF, and RasGAP. To determine which network topology is consistent with our experimental data, we constructed models that incorporate the two known three-node network topologies that can produce perfect adaptation (Figure 2.5A and B) [4, 58]. In the incoherent feedforward topology, Figure 2.5A, both the RasGEF and the RasGAP are activated by the chemoattractant signal acting through the receptors R. Since RasGEF and RasGAP activate and inhibit Ras respectively, this network can have the properties of ultrasensitivity described by Goldbeter and Koshland [36]. In the integral control topology, Figure 2.5B, the output of the model, Ras-GTP, is fed back using the RasGAP as a buffering node. In both models, the external stimulus is translated into an internal response through the binding of the chemoattractant cAMP to the receptors.

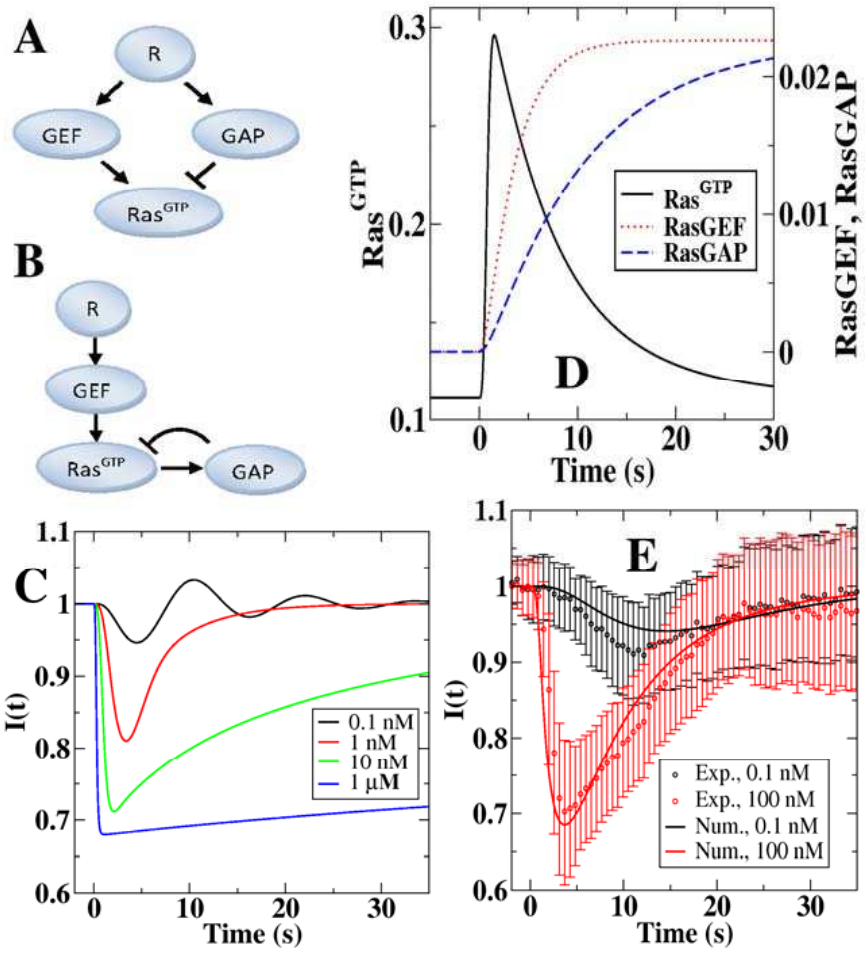

Figure 2.5: Only one possible network topology is consistent with the experimental data. (A) The incoherent feedforward model of Ras adaptation considered in this study. (B) An implementation of the integral control topology. (C) The response of the integral control network, normalized to the pre-stimulus level of RBD-GFP concentration, for different levels of chemoattractant stimulation. (D) A typical time course of the RasGAP, RasGEF, and Ras-GTP for the incoherent feedforward model following a sudden increase in chemoattractant at 0 s. (E) The full dynamical response of RBD-GFP in the experiments (symbols) and in the fitted model (solid lines) for two different concentration increases.

If we assume that the cytosolic concentration of all components is uniform, we can cast the incoherent feed forward model and the integral control model in terms of a set of coupled ordinary differential equations (ODEs). These equations, which describe the dynamics of the concentrations of the components, can then be easily integrated to determine the dynamics of the various components in response to various temporal patterns of the stimulus. For the incoherent feedforward model, the equations take on the form:

$$\begin{aligned}
\frac{dR_1}{dt} &= k_{R1}(cAMP + r_1)(R_1^{tot} - R_1) - k_{-R1}R_1 \\
\frac{dR_2}{dt} &= k_{R2}(cAMP + r_2)(R_2^{tot} - R_2) - k_{-R2}R_2 \\
R &= R_1 + R_2 \\
\frac{dGEF}{dt} &= k_{GEF}R - k_{-GEF}GEF \\
\frac{dGAP}{dt} &= k_{GAP}R - k_{-GAP}GAP \\
\frac{dRas^{GTP}}{dt} &= k_{Ras}GEF(Ras^{tot} - Ras^{GTP}) - k_{-Ras}GAP\, Ras^{GTP} \\
\frac{dRBD^{cyt}}{dt} &= k_{RBD}^{off}(RBD^{tot} - RBD^{cyt}) - k_{RBD}^{on}Ras^{GTP}RBD^{cyt}
\end{aligned}$$

The first two equations describe the binding process of the external chemoattractant, cAMP, to the two receptor populations, R_1 and R_2. One population has a large K_d value and one has a small K_d value. The downstream activity of the bound receptors is assumed to be the same for both populations, such that the effective input in the equations for the downstream components is simply the sum, R. Also, we have allowed for the possibility of constitutive activation, parameterized through r_1 and r_2. The fourth and fifth equations describe the first order activation and deactivation of RasGEF and RasGAP (denoted for brevity by GEF and GAP), while the sixth equation models the dynamics of activated Ras, denoted here as RasGTP. The total concentration of Ras is given by Ras^{tot}. The final equation describes the cytosolic reporter molecule RBD-GFP, denoted by RBD^{cyt}. Its total concentration is RBD^{tot} and it binds membrane-bound activated Ras, leading to

a removal from the cytosol, and is removed from the membrane with simple first order kinetics.

The equations for the integral control model are identical to the ones above, with the equation for RasGAP replaced by

$$\frac{dGAP}{dt} = k_{GAP} Ras^{GTP} - k_{-GAP}.$$

This form of the equations contains a zero-order term, and can be derived from the full Michaelis-Menten kinetic equations assuming saturation conditions. In fact, the full Michaelis-Menten kinetics equation for GAP can be written as

$$\frac{dGAP}{dt} = k_{GAP} Ras^{GTP} \frac{(1 - GAP)}{K_1 + (1 - GAP)} - k_{-GAP} \frac{GAP}{K_2 + GAP}$$

where K_1 and K_2 are the Michaelis constants. When $K_1 << 1 - GAP$ and $K_2 << GAP$, this equation can be approximated by the zero order kinetics as above, while for $K_1 << 1 - GAP$ and $K_2 >> GAP$, it is described by a first order equation. We have verified through direct simulations that the system with full Michaelis-Menten kinetics shows quantitatively similar behavior (Figure 2.6). In particular, it also displays a return to the basal level that becomes progressively slower as the stimulus strength is increased. This is shown in the figure below, where we plot I(t) for three different values of the cAMP stimulus (parameter values: K1=K2=0.0001).

2.4 Data fitting

To compare the dynamic response of the two topologies to the experimental results, we performed mathematical fits using a subset of the experimental data. We chose 21 discrete experimental points that best characterize the experimental data set. Specifically, we chose 5 points from the dose response curve for the non-pretreated cells but excluded the response of non-pretreated cells to a 1 μM stimulus since we have used this value to normalize our results. Furthermore, we picked the 3 points of the dose-response curve for cells pretreated with 100 nM cAMP (Figure 2.3C). The fit also uses the equivalent 8 points of the time

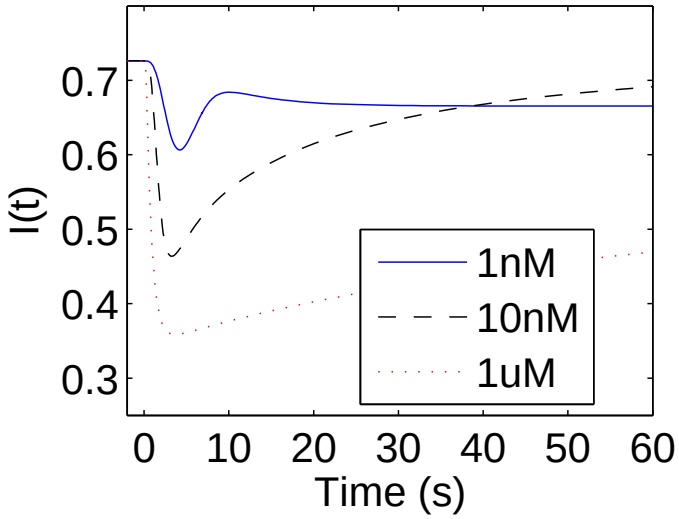

Figure 2.6: Integral control model with full Michaelis-Menten kinetics shows quantitatively similar behavior.

response curves (Figure 2.3D). Note that to avoid overfitting the data, used only two data sets from Figure 2.3C and D (non-pretreated cells and cells pretreated with 100 nM). The resulting 16 points were supplemented by 5 points from the 2 experiments shown in Figure 2.3E and F (0 to 0.2 nM, followed by 0 nM and 100 nM to 1 μM, followed by 100 nM). These are the peak amplitudes, estimated to be 1.0905 and 1.1196, and peak times, taken to be 19.5 sec and 8 sec, following a decrease in the cAMP concentration. Finally, the last point used in our fit was the amplitude of the response 60 sec after a change in concentration from 0.2 nM to 0, estimated to be equal to 1 (Figure 2.3E).

Our model contains 18 parameters, of which we fixed 9: we chose the off rates of the 2 receptors populations to be equal to the values found in single molecule experiments [91]: k_{-R1}=0.16 s^{-1} and k_{-R2}=1.1 s^{-1}. Furthermore, we fixed k_{R1} and k_{R2} by taking the disassociation constant for the high affinity receptor population to be 60 nM and for the low affinity population to be 450 nM, consistent with experimental values [93]. We further reduced the number of free parameters by noticing that k_{GEF} does not affect the kinetics of GEF activation

and is only related to the amount of GEF, which translates into the strength of Ras activation. Since k_{Ras} has the same role to regulate the Ras activation, we simply took k_{GEF}=0.1 k_{-GEF}. Similarly, we fixed $k_{GAP} = 0.1k_{-GAP}$. Moreover, since k_{-GAP} should always be smaller than k_{-GEF}, and since the system is primarily sensitive to the ratio of the 2 parameters, we used with $\ln(k_{-GEF}/k_{-GAP})$ instead of k_{-GAP} as a fitting parameter. Finally, we normalized the Ras and RBD concentration so that $Ras^{tot} = 1$ and $RBD^{tot} = 1$. The model equations were integrated in time until a steady state was obtained. The resulting numerical values of the N=21 fit points, x_i^{sim}, were then compared to the experimental values, x_i^{exp}, using the following error function

$$E = \frac{1}{N}\sum_{i=1}^{21}\left(\frac{x_i^{sim} - x_i^{\exp}}{\sigma_i^{\exp}}\right)^2,$$

where σ_i^{exp} (i=1, 2, $\cdots$, 21) are standard deviations of the experimental data for each fit point. The task is to search for the parameter set k that minimizes E:

$$\mathbf{k} = \arg\min_{\mathbf{k}}(E).$$

In sum, we used 21 data points to constrain the 8 free model parameters. Since the resulting 9-dimensional parameter space can have numerous local minima, we chose simulated annealing as our method of fitting. Unlike other algorithms, simulated annealing samples a large region of parameters space and do not reject parameter choices that do not improve the fit [74]. This is done via assigning an artificial temperature and "cooling" the system. Specifically, we started from a high temperature (T=3000), performed 100 parameter searches at each iteration and reduced the temperature by 10% after each iteration. Our program ended when the step size in the parameter space became smaller than a defined cut-off small or when the temperature has been decreased for 100 times, whichever comes first. To enlarge the searchable area in parameter space, we started the program from different initial conditions. The resulting parameters, corresponding to a fit with E=0.12, are shown in Table 2.1. We have also performed fits using different experimental data points and slightly different versions of the model equations. For example, in one fit we have used all the data from Figure 2.3C-F while in another fit we excluded the possibility of constitutive activation of the receptors (i.e.,

Table 2.1: Model parameters in feedforward model

parameter	value
R_1^{tot}	0.1
R_2^{tot}	0.9
k_{R1}	0.00267 $nM^{-1}sec^{-1}$
k_{-R1}	0.16 sec^{-1}
k_{R2}	0.00244 $nM^{-1}sec^{-1}$
k_{-R2}	1.1 sec^{-1}
r_1	0.012 nM
r_2	0.115 nM
k_{GEF}	0.04 sec^{-1}
k_{-GEF}	0.4 sec^{-1}
k_{GAP}	0.01 sec^{-1}
k_{-GAP}	0.1 sec^{-1}
Ras^{tot}	1
k_{Ras}	390 sec^{-1}
k_{-Ras}	3126 sec^{-1}
RBD^{tot}	1
k_{RBD}^{off}	0.53 sec^{-1}
k_{RBD}^{on}	1.0 sec^{-1}

r_1=0 and r_2=0). These fits were found to still duplicate the experimental data well, with an error function that was less that 0.3. Furthermore, the parameters that were selected were always close to the ones shown in Table 2.1, indicating that our fitting is not highly sensitive to the choice of fit points or the specific details of the model. This is not surprising, since the experimental data put significant constraints on the possible range of the parameters. In particular, the observed transient depletion of the cytosol following an increase in chemoattractant requires that k_{-GEF} is always larger than k_{-GAP}. Furthermore, k_{-GAP} determines the time scale of the return to basal level and is thus constrained by the experimentally observed values. Also, the peak amplitude of the response limits the allowed ratios of k_{-GAP} and k_{-GEF}. Finally, the fraction of low affinity receptors, R_2^{tot}, needs to be large since there is a significant response in cells pre-treated with 100 nM.

2.5 Response time in the two adaptation models

Our simulation results indicate that the integral control mechanism is incompatible with our experimental results. In particular, this mechanism displays a significant dependence of the adaptation kinetics on the size of the stimulus step. This is shown in Figure 2.5C, where we plot the response of our integral feedback model to a range of stimulus steps. Contrary to our experimental results, for small concentration increases this network leads to oscillations and, more importantly, the time to reach the basal level increases markedly as the step size increases.

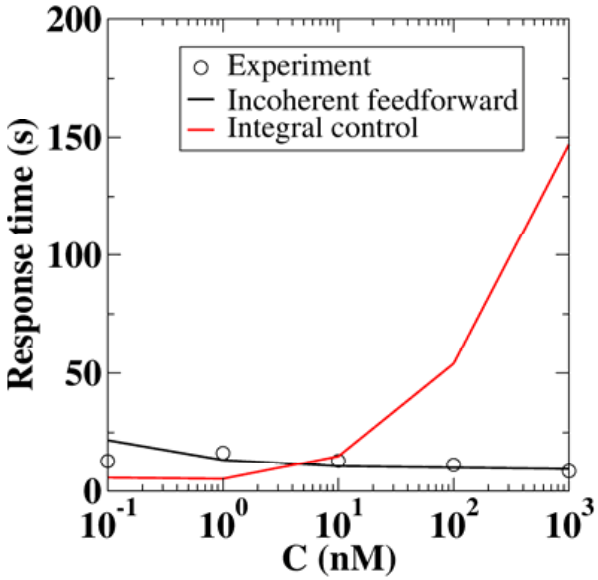

Figure 2.7: The response time for the incoherent feedforward model (black line), the integral control model (red line), and found in the experiments (symbols) as a function of the chemoattractant step size.

The results of the best fit using the incoherent feedforward network are shown as solid lines in Figure 2.3C and D. In contrast to the integral control topology, the RBD-GFP level in the incoherent feedforward model can respond to a wide range of chemoattractant stimuli and adapts quickly. Specifically, this network topology is able to respond quickly even when the stimulus is large. Furthermore, the numerical results track the experimental data well for all stimulus strengths, including the data sets that were not explicitly fitted. The model pa-

rameters obtained by our fitting procedure are listed in Table 2.1.

To better illustrate the difference between the incoherent feedforward model and the integral control model, we defined the response time for both models as the time between the half-peak value during the rise phase and the half-peak value during the decay phase of the response. In the integral control model, this response time increases as the stimulus size is increased (red line, Figure 2.7). In contrast, the response time decreases for increasing step sizes in the incoherent feedforward model (black line, Figure 2.7), consistent with experimental results (symbols, Figure 2.7).

A closer inspection of the results of our fitting procedure reveals that the RasGEF activation kinetics is faster than that of the RasGAP. This is to be expected since a positive Ras-GTP response following an increase in cAMP requires that the activation step initially is larger than the de-activation step. Eventually, the RasGAP kinetics catches up, resulting in a steady-state Ras-GTP level that is independent of the stimulus strength. The kinetics of our model components is shown in Figure 2.5D where we plot RasGAP, RasGEF, and Ras-GTP as a function of time, following a sudden increase in chemoattractant concentration. In Figure 2.5E, we plot the full dynamical response in our simulations together with experimental results for two jumps in the chemoattractant concentration. Finally, our simulation results for the two experiments in which the concentration is increased and then subsequently decreased are shown as solid lines in Figure 2.3E and F. The agreement between the experiments and the simulations is excellent for the entire time course of the experiments.

2.6 Other topologies with negative feedback

Additionally, other ways to implement integral control are also incompatible with the experimental data. All possible three-node topologies containing a negative feedback loop are shown in Figure 2.8, including ones that are biologically not plausible. The topologies shown in Figure 2.8B-F differ slightly from the core topology discussed above and shown in Figure 2.8. In the topologies of Figure

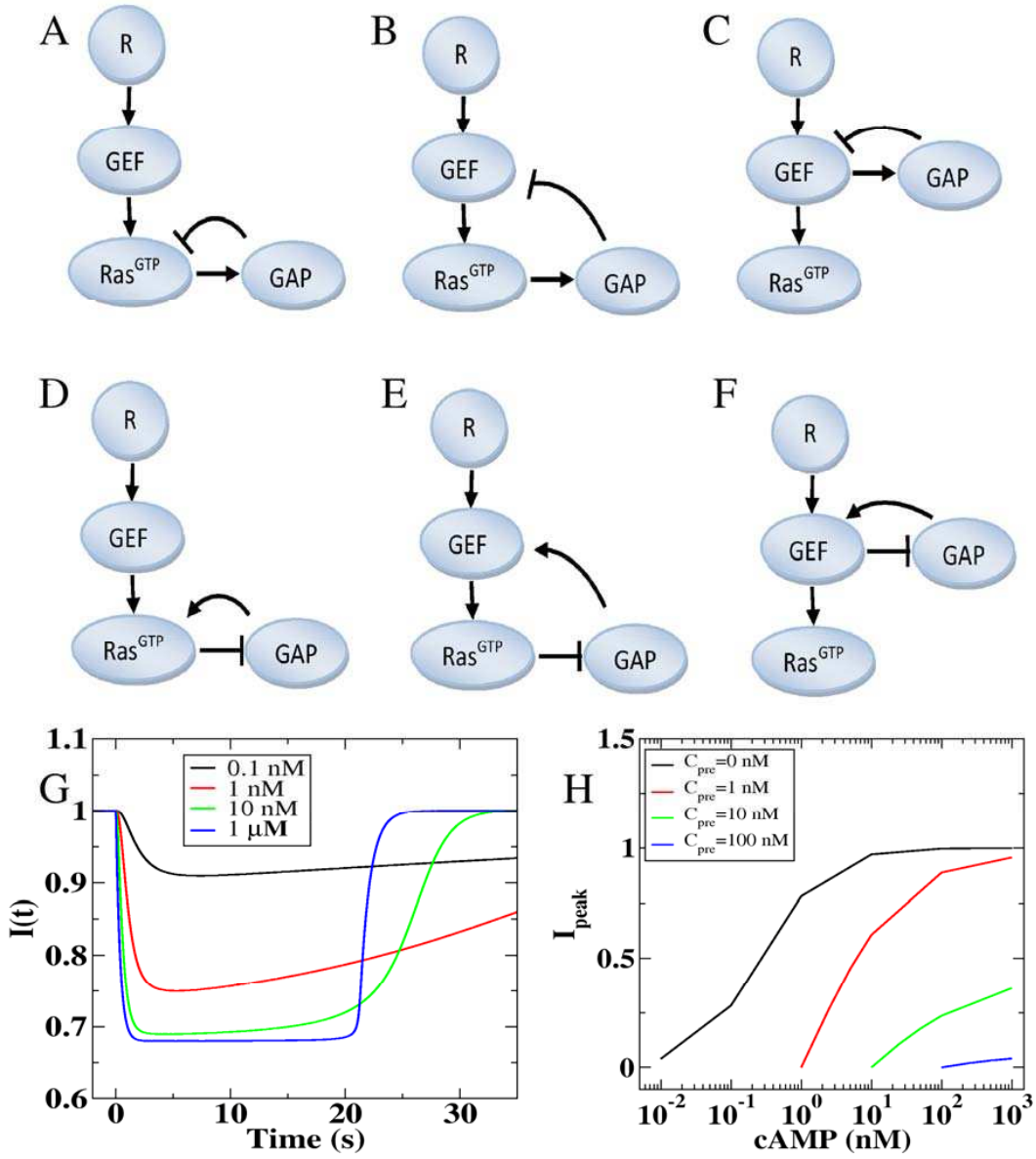

Figure 2.8: All possible integral control topologies (A-F). The dynamics of topology B and C is qualitatively similar to the one depicted in A and discussed in the main text. The qualitative dynamics of topology D-F is shown in G and the corresponding dose-response curves are plotted in H.

2.8A-C, either RasGEF or activated Ras activates RasGAP which, in turn, exerts a negative feedback. Through explicit numerical simulations, we have verified that these three topologies are inconsistent with the experiments for the reasons

described in the main text: the timescale of the return to basal level following an increase in cAMP is proportional to the magnitude of the stimulus. We will give an analytical argument to this effect below. The topologies of Figure 2.8D-F are characterized by the existence of an inhibitory coupling between either RasGEF or activated Ras and RasGAP. The feedback loop is closed through a positive link between RasGAP and RasGEF or activated Ras. These topologies are also inconsistent with the experimental findings. In particular, as we will explain in further detail below, for large values of the stimulus, Ras-GTP saturates and remains close to its maximal value for a prolonged period of time (Figure 2.8G). This would result in experiments with a prolonged plateau in the RBD-GFP intensity. Furthermore, the fact that Ras-GTP saturates makes it impossible to obtain the dynamic range observed in the dose-response experiments. Specifically, it is possible to obtain a dose-response curve that is close to the experimental one for untreated cells. However, since for large values of the concentration Ras-GTP is saturated, the response to a stimulus increase for cells that were pre-treated with a large chemoattractant concentration is very small. This is shown in Figure 2.8H, in which we plot the dose-response curves for different values of initial chemoattractant concentrations. Clearly, there is a very small response of cells pre-treated with 100 nM (blue line) to increases in chemoattractant, inconsistent with the experimental results.

2.7 Analytical analysis of the incoherent feedforward and the integral control topologies

The core of the incoherent feedforward model can be represented by Figure 2.9A, where the input signal S activates both A and B, which control the dynamics of the output X. The equations describing this core motif can be written as

$$\frac{dA}{dt} = k_a S - k_{-a} A \tag{2.1}$$
$$\frac{dB}{dt} = k_b S - k_{-b} B \tag{2.2}$$
$$\frac{dX}{dt} = k_x A(1 - X) - k_{-x} BX. \tag{2.3}$$

where we normalized the X equation by the total amount of X. The steady state values of A and B depend on S,

$$A_0 = \frac{k_a}{k_{-a}} S, B_0 = \frac{k_b}{k_{-b}} S,$$

while the steady state level of X is

$$X_0 = \frac{k_x A_0}{k_x A_0 + k_{-x} B_0}.$$

Thus, since both A_0 and B_0 depend linearly on S, X_0 will be independent of S. A linear stability analysis for the steady state of the system can be carried out. The growth mode λ is given by the solution of the following eigenvalue problem:

$$\begin{vmatrix} -k_{-a} - \lambda & 0 & 0 \\ 0 & -k_{-b} - \lambda & 0 \\ k_x(1 - X_0) & -k_{-x} X_0 & -k_x A_0 - k_{-x} B_0 - \lambda \end{vmatrix} = 0$$

These eigenvalues are always real and negative, demonstrating that the steady state is linearly stable and that X does not exhibit oscillations.

The kinetics of X depends on the amount of A and B present. For small values of S, both A and B are small and the kinetics of X is slow. That is, Eqn.(2.1) and Eqn.(2.2) are much faster than Eqn.(2.3) and we can approximate A and B by their quasi-steady state values:

$$A \sim \frac{k_a}{k_{-a}} S, B \sim \frac{k_b}{k_{-b}} S.$$

Then, Eqn.(2.3) can be written as

$$\frac{1}{S}\frac{dX}{dt} = \frac{k_x k_a}{k_{-a}}(1 - X) - \frac{k_{-x} k_b}{k_{-b}} X$$

Thus, the timescale of recovery for X, τ, is inversely proportional to the signal strength, $\tau \sim 1/S$. On the other hand, when S is large, Eqn.(2.3) equilibrates quickly and

$$X \sim \frac{k_x A}{k_x A + k_{-x} B}.$$

Since both A and B are linearly dependent on S,

$$A = \frac{k_a}{k_{-a}} S(1 - e^{-k_{-a}t})$$

and

$$B = \frac{k_b}{k_{-b}} S(1 - e^{-k_{-b}t}),$$

we find that the kinetics of X are independent of S.

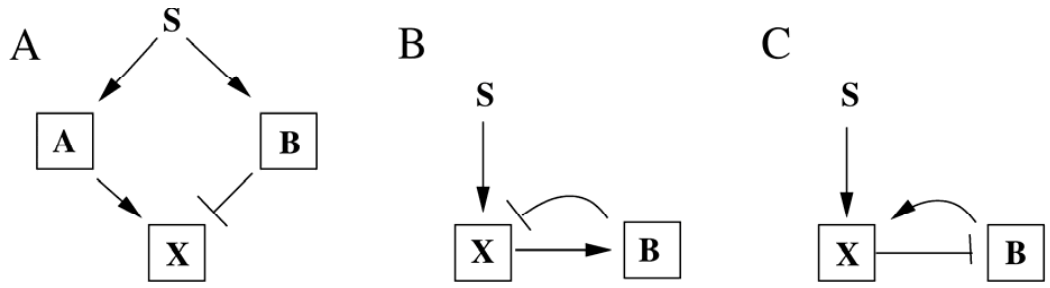

Figure 2.9: (A) Basic motifs of incoherent feedforward model. (B) and (C) Integral control (negative feedback) model. S is the input signal, and X is the output.

The integral control models, with negative feedback, can be represented by two core motifs. For analytical convenience, we assume that the activation of activator A is fast compared to the timescales for B and X. Then, these motives reduces to two-node topologies and in the first one (Figure 2.9B), the buffering node is activated by X and deactivates X:

$$\frac{dX}{dt} = k_x S(1 - X) - k_{-x} B X \tag{2.4}$$

$$\frac{dB}{dt} = k_b X - k_{-b} \tag{2.5}$$

The zero-order terms in these equations, and in the ones for the second motif below were chosen to facilitate the analytical treatment and can be derived

in certain limits of the full Michaelis-Menten kinetic equations. We have verified through numerical simulations that the system with full Michaelis-Menten dynamics shows qualitatively similar behavior.

The steady state levels can be easily found to be

$$X_0 = \frac{k_{-b}}{k_b}$$

and

$$B_0 = \frac{k_x S(1 - X_0)}{k_{-x} X_0}.$$

A linearization around these steady state values gives as the growth modes:

$$\begin{vmatrix} -k_x S - k_{-x} B_0 - \lambda & -k_{-x} X_0 \\ k_b & -\lambda \end{vmatrix} = 0 \Rightarrow \lambda^2 + (k_x S + k_{-x} B_0)\lambda + k_{-x} k_{-b} = 0.$$

Imaginary values for these modes will result in oscillations in the value of X for constant S. To avoid these oscillations, one has to choose k_{-b} small enough.

When Eqn. (2.4) is much faster than Eqn. (2.5), we can approximate B by its quasi-steady state value

$$B \sim \frac{k_x S(1 - X)}{k_{-x} X}$$

. Then,

$$\frac{dB}{dt} = -\frac{k_x S}{k_{-x} X^2} \frac{dX}{dt} = k_b X - k_{-b}$$

and

$$S \frac{dX}{dt} = -\frac{k_{-x}}{k_x} X^2 (k_b X - k_{-b})$$

Thus, the recovery time scale increases with S: $\tau \sim S$, inconsistent with the experimental results.

In the second motif (Figure 2.9C), the buffering node B activates X and is deactivated by X. Since B is not activated by the signal, we will assume a constant constitutive activation. To obtain a non-trivial dynamics, it is necessary to have activation of B in the absence of a signal, leading to the following set of equations:

$$\frac{dX}{dt} = k_x (S + c) B (1 - X) - k_{-x} X \tag{2.6}$$

$$\frac{dB}{dt} = k_b - k_{-b} X \tag{2.7}$$

with steady-state values

$$X_0 = \frac{k_b}{k_{-b}}$$

and

$$B_0 = \frac{k_{-x}\frac{k_b}{k_{-b}}}{k_x(S+c)(1-\frac{k_b}{k_{-b}})}.$$

The linear stability is found by solving

$$\begin{vmatrix} -\frac{k_{-x}}{1-\frac{k_b}{k_{-b}}} - \lambda & k_x(S+c)(1-\frac{k_b}{k_{-b}}) \\ -k_{-b} & -\lambda \end{vmatrix} = 0$$

leading to

$$\lambda^2 + \frac{k_{-x}}{1-\frac{k_b}{k_{-b}}}\lambda + k_x(S+c)(k_{-b}-k_b) = 0.$$

Thus, again, the kinetics of the buffering node B, characterized by k_{-b}, needs to be slow to avoid oscillations. Then, Eqn. (2.6) will equilibrate quickly, and

$$X \approx \frac{k_x(S+c)B}{k_x(S+c)B + k_{-x}}.$$

For large values of S, X reaches its peak $X_{peak} \sim 1$ (Figure 2.8G) and remains saturated for a prolonged period. During this time, the decay rate of B is about

$$\frac{dB}{dt} \approx k_b - k_{-b},$$

leading to

$$\frac{dX}{dt} \approx \frac{k_x k_{-x}(S+c)}{[k_x(S+c)B + k_{-x}]^2}\frac{dB}{dt} \approx \frac{k_x k_{-x}(S+c)}{[k_x(S+c)B_0 + k_{-x}]^2}(k_b - k_{-b}).$$

Therefore, the decay of X right after X_{peak} gets slower when S increases.

2.8 Inclusion of two receptors

Previous studies have identified several species of receptors with different binding affinities for cAMP [93]. Thus, we include two types of receptors in our models, one with a high affinity (R_1, dissociation constant K_d^1=60 nM) and one with a low affinity (R_2, K_d^2=450 nM). We assume that the two types of receptors

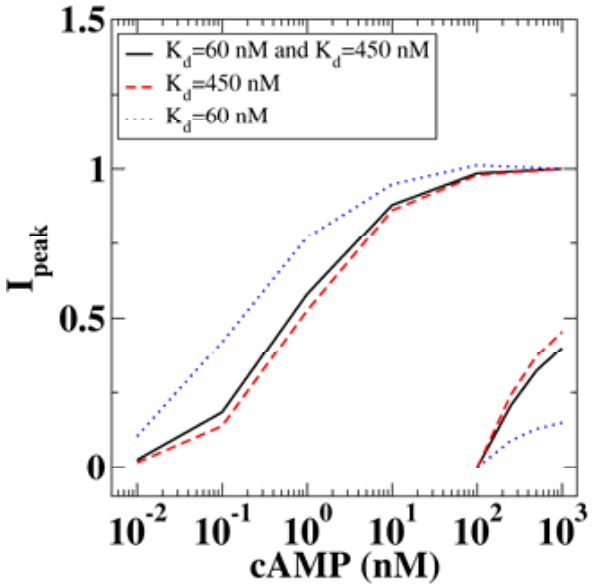

Figure 2.10: Numerical dose response curves for cells with only low affinity (K_d=450 nM; red dashed lines) or only high affinity (K_d=60 nM; blue dotted lines) receptors. Shown are the results without any pre-stimulus and with a 100 nM pre-stimulus. The solid curves are shown for comparison and represent the simulations results of the mixed receptor population described in the main text.

activate downstream components in an identical fashion. Numerical fits with only one receptor population result in dose-response curves that are less accurate. This is demonstrated in Figure 2.10, in which we show the results of our simulations if only the low affinity (dashed lines) or the high affinity receptor population (dotted lines) is included. As a comparison, we have also plotted our simulations results for the two-population receptor model. Inclusion of only the low affinity receptors leads to a reduced response for small values of the stimulus in the non-pretreated cells. The effect of only high affinity receptors is more dramatic, as it increases the response at low values in the non-pretreated cells. Furthermore, it greatly reduces the response in cells that are pretreated with 100 nM cAMP. We have also calculated the Akaike's information criterion, AIC, a measure of the relative goodness of fit. This criterion is expressed as

$$AIC = 2k + \xi^2,$$

where k is the number of fitting parameters. We found the following values for this criterion: AIC=20.5 (for the model with both receptor populations), AIC=31 (with only the K_d=60 nM receptors), and AIC=17.5 (with only the K_d=450 nM receptors). This indicates that a model with either both or only the low affinity receptors gives a better a fit than the model with only the high affinity receptors.

2.9 Effect of potential positive feedbacks

In addition, we have verified that including a feedback from Ras to RasGEF, as suggested in previous studies [20], does not change the qualitative results of the model (Figure 2.11). Specifically, we changed the GEF equation to

$$\frac{dGEF}{dt} = k_{GEF}R(1 + \frac{a_{fb}Ras}{K_{fb} + Ras}) - k_{-GEF}GEF$$

where the feedback strength is determined through the parameter a_{fb}. Again, the time scale for the return to basal level increases as the stimulus strength is increased, as shown in the figure below (parameter values: a_{fb}=10 and K_{fb}=0.1).

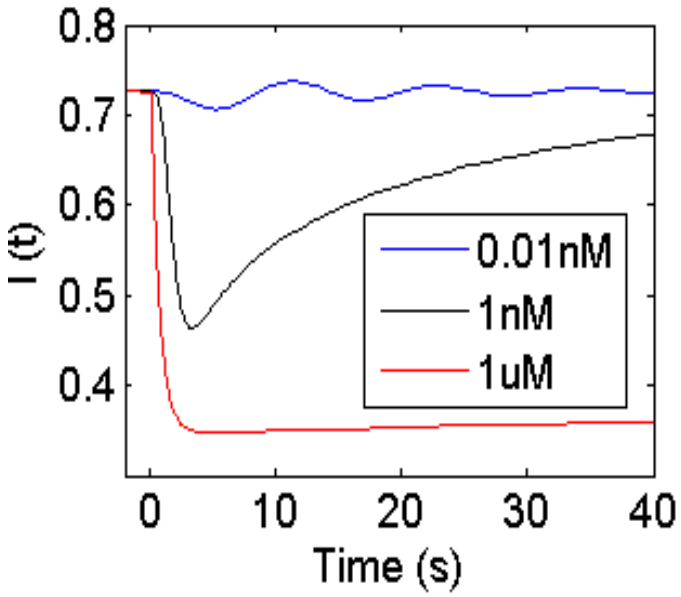

Figure 2.11: Including a feedback from Ras to RasGEF does not change the qualitative results of the model

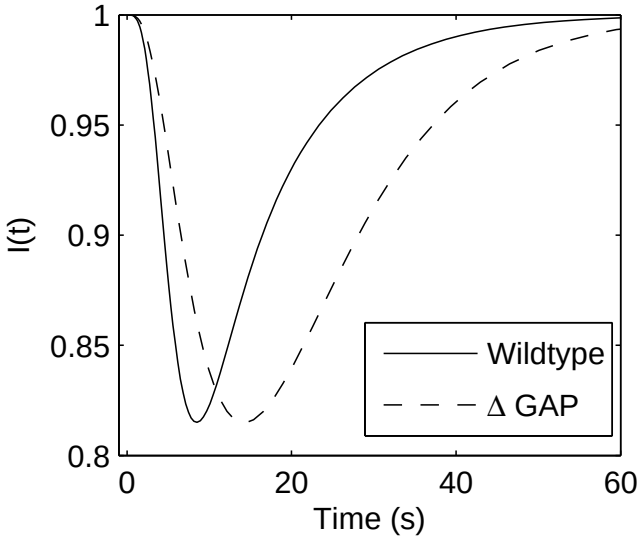

Figure 2.12: Predicted behavior of GAP mutants. cAMP concentration is 1nM. The solid curve represents the wild type cell, while the dashed curve is for the GAP-mutant. In simulation, the parameter k_{-Ras} is decreased by 100 folds for the mutant.

2.10 Prolonged response in GAP mutants

To study the behavior of GAP mutant, we decrease the parameter k_{-Ras}, which captures the inhibition strength of GAP, by 100 folds. The response in the feedforward model is prolonged (see Figure 2.12) which is consistent with experimental observation [108]. However, the response in the integral control model is also prolonged in the similar way, so the behavior of GAP mutants cannot distinguish the two models.

2.11 Spatially extended models

A spatially extended version of the adaptation model can be formulated in a straightforward manner. In this spatially extended version of the LEGI model, both GAP and RBD^{cyt} diffuse in the cytosol with diffusion constants D_{GAP} and

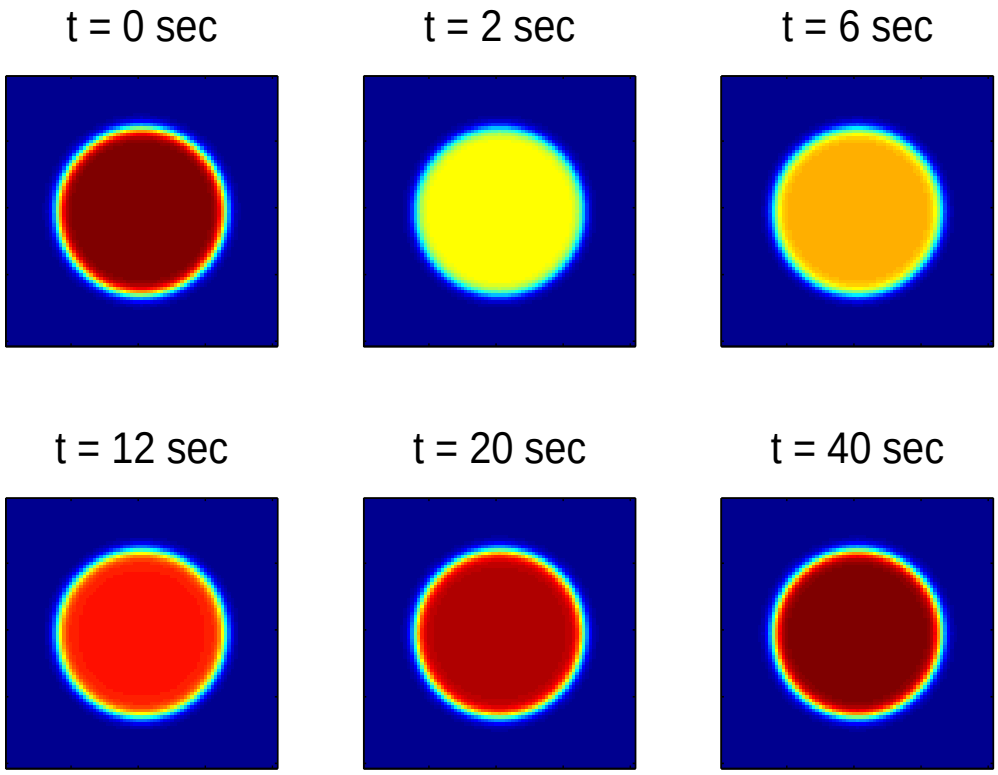

Figure 2.13: The evolution of cytosolic RBD-GFP in response to a sudden increase in chemoattractant from 0 to 1 μM.

D_{RBD}, respectively. The above equations for the receptors and GEF are unchanged while the remaining equations now describe the concentration in the cytosol and on the membrane in terms of partial different equations (PDEs):

$$\frac{dGAP^{mem}}{dt} = k_{GAP}^{on} GAP^{cyt} - k_{-GAP} GAP^{mem}$$
$$\frac{\partial GAP^{cyt}}{\partial t} = D_{GAP} \nabla^2 GAP^{cyt}$$
$$\frac{dRas^{GTP}}{dt} = k_{Ras} GEF(Ras^{tot} - Ras^{GTP}) - k_{-Ras} GAP^{mem} Ras^{GTP}$$
$$\frac{dRBD^{mem}}{dt} = k_{RBD}^{on} Ras^{GTP} RBD^{cyt} - k_{RBD}^{off} RBD^{mem}$$
$$\frac{\partial RBD^{cyt}}{\partial t} = D_{RBD} \nabla^2 RBD^{cyt}$$

These equations need to be supplemented with the boundary conditions

$$D_{GAP}\frac{\partial GAP^{cyt}}{\partial n} = k_{GAP}R - k^{on}_{GAP}GAP^{cyt}$$
$$D_{RBD}\frac{\partial RBD^{cyt}}{\partial n} = -k^{on}_{RBD}Ras^{GTP}RBD^{cyt} + k^{off}_{RBD}RBD^{mem}$$

where n is the normal to the cell membrane.

We have simulated these equations, representing a spatially extended implementation of the Local Excitation, Global Inhibition (LEGI) model, using a disk-shaped cell with radius R=5 μm (Figure 2.13). The resulting RBD^{cyt} dynamics, following an increase in cAMP, is shown in Figure 2.14 as symbols. The corresponding RBD^{cyt} dynamics for the case where the cytosolic RBD-GFP concentration is assumed to be uniform and the equations can be described by ODEs is plotted as a solid line. A comparison reveals that both models display the same quantitative behavior. Of course, this result is not surprising since, as long as D_{RBD} is large enough, the spatial variations of RBD^{cyt} will be negligible. This result is also consistent with our experimental finding that changing the cytosolic region in which we measure the fluorescence intensity does not appreciably alter our results.

2.12 Discussion

Our study examines the initial response to changes in uniform chemoattractant stimuli using a combined experimental and theoretical approach. We did not consider possible responses with longer time scales, including the formation of Ras patches and cell polarization. We find that the response of activated RasG adapts perfectly for a large range of cAMP stimuli, in particular for stimuli less than 1 μM. The inclusion of GEF saturation in our model can account for the possibe deviation from perfect adaptation for very large stimuli. We also find that the peak time of the response of activated RasG decreases with increasing stimulus concentration. This is consistent with previous experiments on the kinetics of membrane-bound PIP3, a signaling component downstream from activated Ras, which showed that the peak value for PIP3 is reached faster for a high value of

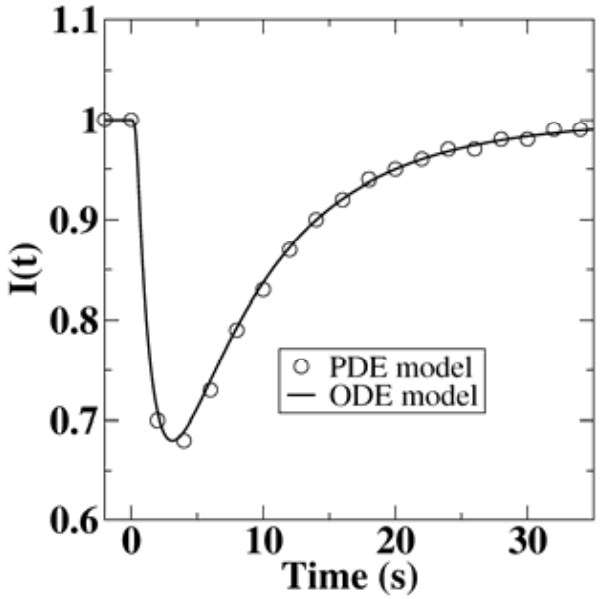

Figure 2.14: The cytosolic RBD-GFP, normalized by RBD^{cyt} before simulation, as a function of time following a sudden increase in chemoattractant from 0 to 1 μM for the spatially uniform model governed by ODEs (solid line) and the spatially extended model described by PDEs (symbols). The common parameters for both models are given in Table 2.1 while the additional parameters for the spatially extended model are: $D_{GAP} = 30\mu m^2/s$, $D_{RBD} = 10\mu m^2/s$, $k^{on}_{GAP} = 3\mu m/s$.

cAMP stimulus (100 nM) that for a low value of cAMP (1 nM) [101]. Our combined experimental and theoretical analysis suggests that adaptation in the RasG signaling pathway does not rely on integral control mechanisms that contain negative feedback loops. Instead, and unlike any other biological systems analyzed to date, adaptation is achieved through the simultaneous activation of an activator and inhibitor. In the model we have analyzed here, the signal directly activates RasGEF and RasGAP and variants of the incoherent feedforward topology (Figure 2.15) will give similar results. Of course, an alternate possibility is that adaptation is achieved downstream from the receptors and upstream from RasGEF. The output of this adaptation module, containing unknown components, would then activate RasGEF while RasGAP is constitutively active. In either case, our network is consistent with the Local Excitation, Global Inhibition (LEGI) model [70] for gradient sensing that postulates that the response to an external chemoat-

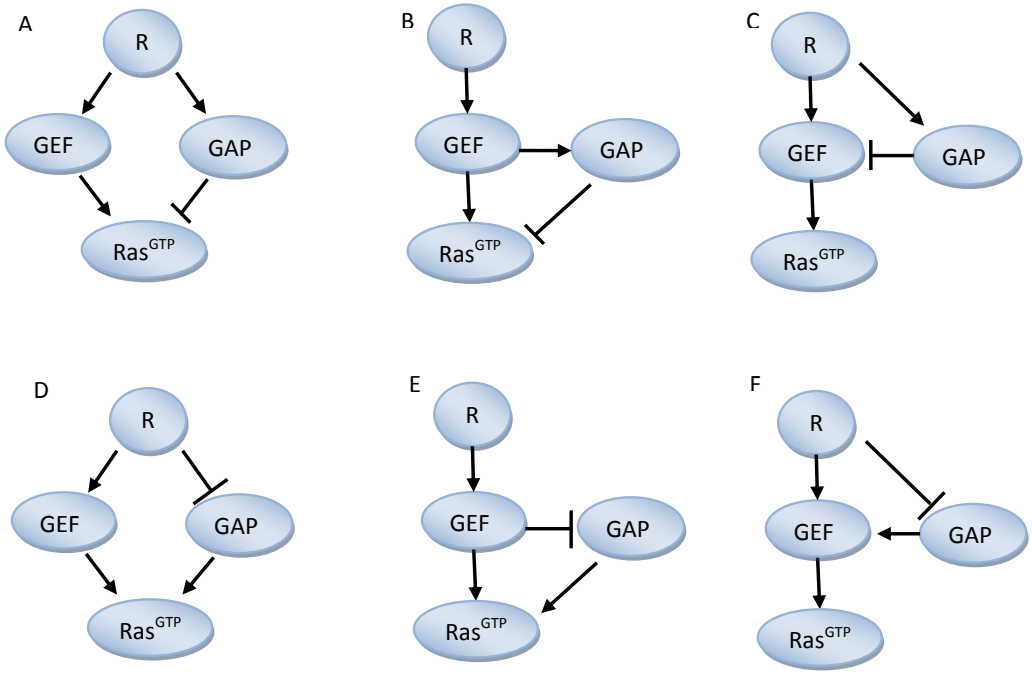

Figure 2.15: Theoretically possible implementations, including ones that are biologically not plausible, of the incoherent feedforward model. The topology in A is the one we employ in this study.

tractant signal is governed by an intracellular membrane-bound activator and an inhibitor that is diffusing throughout the cell. Such a gradient sensing model can convert the external gradient of bound receptors into an internal gradient, especially if it is coupled to a module that further amplifies the internal asymmetry [38, 100]. Our model suggests that the activator RasGEF is the local, membrane bound component while the inhibitor RasGAP is the diffusive cytosolic component. This is consistent with previous results showing that the RasG-GAP *Dictyostelium* NF1 is an essential and uniformly distributed component of the directional sensing mechanism and that in the absence of NF1, cells are unable to effectively sense the chemoattractant gradient's direction and exhibit extended RasG activation [108]. Further, our results argue that the RasG-GAP is not constitutively active but is activated in response to chemoattractant stimulation and that this activation of both the RasGEF and the RasGAP is essential for gradient sensing and adaptation.

2.13 Acknowledgements

We thank Peter Van Haastert for providing us with the Raf-GFP cells. This work was supported by the US National Institutes of Health (PO1 GM078586). This chapter is based on the following paper:

K. Takeda, D. Shao, M. Adler, P. G. Charest, W. F. Loomis, H. Levine, A. Groisman, W. J. Rappel and R. A. Firtel. Incoherent feedforward control governs adaptation of activated Ras in a eukaryotic chemotaxis pathway. *Submitted to Science Signaling.*

2.14 Appendix

Materials and methods. Transformed KAx-3 cells carrying an extrachromosomal construct in which the regulatory region of Actin 15 drives a fusion of GFP to the Ras binding domain of Raf were grown in suspension in HL5 medium. When exponentially growing cells reached $1-3\times10^6$ cells/ml, they were harvested by centrifugation, washed in phosphate buffer, and resuspended in phosphate buffer at 5×10^6 cells/ml. Shaken cells were starved for 1 h before addition of pulses of 30 nM cAMP every 6 min for 5 h.

Chapter 3

Applying phase field method to cell biology

3.1 Introduction

Phase field method is an effective tool to solve moving boundary problems.It has been successfully applied to wide ranging problems such as solidification [75], crack propagation [47], viscous fingering [30] and diffusional problems in complicated geometries [28, 49].

To describe a cell, phase field method introduces an auxiliary field ϕ. We define the free energy

$$F[\phi] = \int \frac{1}{\epsilon}[\frac{(\epsilon|\nabla\phi|^2)}{2} + G]d\mathbf{r},$$

where $\frac{\epsilon}{3}$ characterizes the width of the sharp interface and it must satisfy

$$\Delta x < \frac{\epsilon}{3} \ll r.$$

Here Δx is the grid size in the computing space, and r is the cell size. Previous study has proved that ϵ does not have to be too large over Δx and $\frac{\epsilon}{3} > 2\Delta x$ is able to produce results to sufficient precision [49]. G is a double well potential (see Figure 3.1)

$$G = 18\phi^2(1-\phi)^2.$$

G has two minima $\phi = 0$ and $\phi = 1$, which can be used to distinguish the cell from the environment. For example, let $\phi = 1$ denote the interior of the cell and

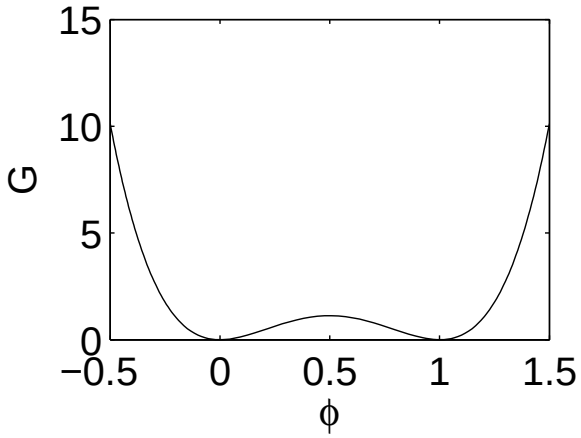

Figure 3.1: Double well potential for the phase field.

$\phi = 0$ the external area. The diffuse layer separating the interior from the exterior marks the membrane location. The dynamics of the cell is governed by equations that couple this field to the actual physical degrees of freedom. Importantly, this technique does not require the explicit tracking of this boundary. The phase field method presented in this chapter will be used in Chapter 4 and Chapter 5.

3.2 Interface energy

Consider a simple case, where a vesicle only possesses the interface energy. From variational relation, we get

$$\epsilon \frac{\partial \phi}{\partial t} = -\frac{\delta F[\phi]}{\delta \phi}$$

In one dimension, the right hand side can be calculated as

$$\begin{aligned} \frac{\delta F}{\delta \phi} &= \epsilon \int \nabla \phi \frac{\nabla \delta \phi}{\delta \phi} dx' + \frac{1}{\epsilon} \int G'[\phi(x')] \frac{\delta \phi(x')}{\delta \phi(x)} dx' \\ &= -\epsilon \int \nabla^2 \phi \frac{\delta \phi(x')}{\delta \phi(x)} dx' + \frac{1}{\epsilon} G' \\ &= -\epsilon \nabla^2 \phi + \frac{1}{\epsilon} G' \end{aligned}$$

Therefore,

$$\epsilon \frac{\partial \phi}{\partial t} = \epsilon \nabla^2 \phi - \frac{1}{\epsilon} G'$$

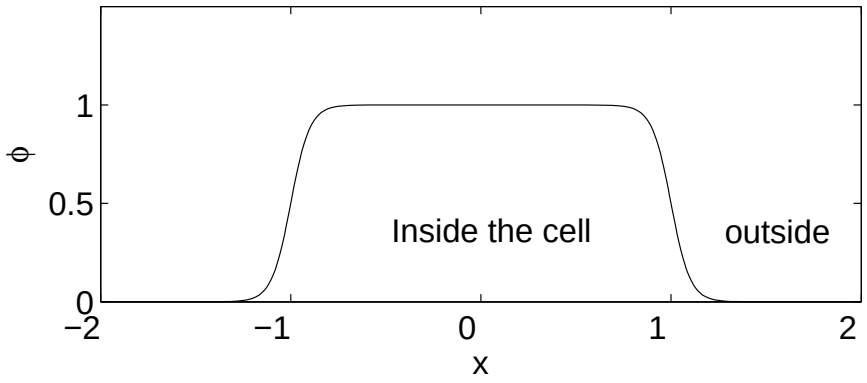

Figure 3.2: Phase field for a one dimensional vesicle.

At stationary state, the above equation equals zero, and its solution is

$$\phi = \frac{1}{2} + \frac{1}{2}\tanh\frac{3d}{\epsilon},$$

where d is the signed distance from the nearest boundary ($d > 0$: inside the cell; $d < 0$: outside the cell). Figure 3.2 illustrates a stationary one-dimension vesicle.

However, if we move from one dimension to two dimension, the vesicle with only the interface energy will shrink. Actually,

$$\begin{aligned}
\nabla\phi &= \hat{n}\frac{\partial\phi}{\partial n} \\
\nabla^2\phi &= \hat{n}\cdot\frac{\partial}{\partial n}(\hat{n}\frac{\partial\phi}{\partial n}) = \frac{\partial^2\phi}{\partial n^2} + \frac{\partial\phi}{\partial n}(\nabla\cdot\hat{n}) \\
\epsilon\frac{\partial\phi}{\partial t} &= \epsilon\frac{\partial^2\phi}{\partial n^2} - \frac{G'}{\epsilon} + \epsilon\frac{\partial\phi}{\partial n}(\nabla\cdot\hat{n}) = 0 - \epsilon c|\nabla\phi|
\end{aligned}$$

with curvature $c = -\nabla\cdot(\frac{\nabla\phi}{|\nabla\phi|})$. As long as the curvature is positive, the circle will shrink, and the shrinking speed $v \sim \epsilon^2 c$ [9]. To get a stationary vesicle, the interface energy must be balanced. For example [8],

$$\epsilon\frac{\partial\phi}{\partial t} = \epsilon\nabla^2\phi - \frac{G'}{\epsilon} + \epsilon c|\nabla\phi|$$

3.3 Vesicle shapes with fixed area and volume

This work was inspired by Seifert's theoretical work on fluid membranes and vesicles [85]. Consider a vesicle with fixed area A_0, fixed volume V_0 and spontaneous curvature c_0, its free energy can be written as

$$F[\phi] = F_B[\phi] + F_V[\phi] + F_A[\phi]$$

Here, the volume energy is described by

$$F_V[\phi] = \frac{M_V}{2}(V - V_0)^2$$

where

$$V = \int \phi d\mathbf{r}.$$

Thus, the prescribed volume $V = V_0$ gives the minimum volume energy.

Similarly, the area energy can be written as

$$F_A[\phi] = \frac{M_A}{2}(A - A_0)^2$$

where

$$A = \int [\frac{\epsilon}{2}|\nabla\phi|^2 + \frac{1}{\epsilon}G]d\mathbf{r}.$$

The bending energy takes the form

$$F_B[\phi] = \frac{b_N}{2}\oint (c - c_0)^2 dA$$

Since

$$\epsilon\nabla^2\phi - \frac{1}{\epsilon}G' = -\epsilon c|\nabla\phi|$$

The above equation is actually

$$F_B[\phi] = \frac{b_N}{2}\int \frac{1}{\epsilon}[\epsilon\nabla^2\phi - \frac{1}{\epsilon}G' + c_0 6\phi(1-\phi)]^2 d\mathbf{r}$$

From the variational relation, we then get the evolution of ϕ

$$\epsilon\frac{\partial\phi}{\partial t} = -\frac{\delta F[\phi]}{\delta\phi}$$

The right hand side can be expanded as

$$\frac{\delta F_V[\phi]}{\delta\phi} = M_V(V - V_0)$$

$$\frac{\delta F_A[\phi]}{\delta \phi} = -M_A(A - A_0)(\epsilon \nabla^2 \phi - \frac{1}{\epsilon} G')$$
$$\frac{\delta F_B[\phi]}{\delta \phi} = \nabla^2 w - \frac{1}{\epsilon^2} G'' w + \frac{c_0}{\epsilon} 6(1 - 2\phi) w$$

where

$$w = b_N(\epsilon \nabla^2 \phi - \frac{1}{\epsilon} G' + 6\phi(1 - \phi)c_0).$$

Note that we need to solve a 4th order partial differential equation, which is computationally intense. We use ADI (Alternating Directional Implicit) method (see Appendix).

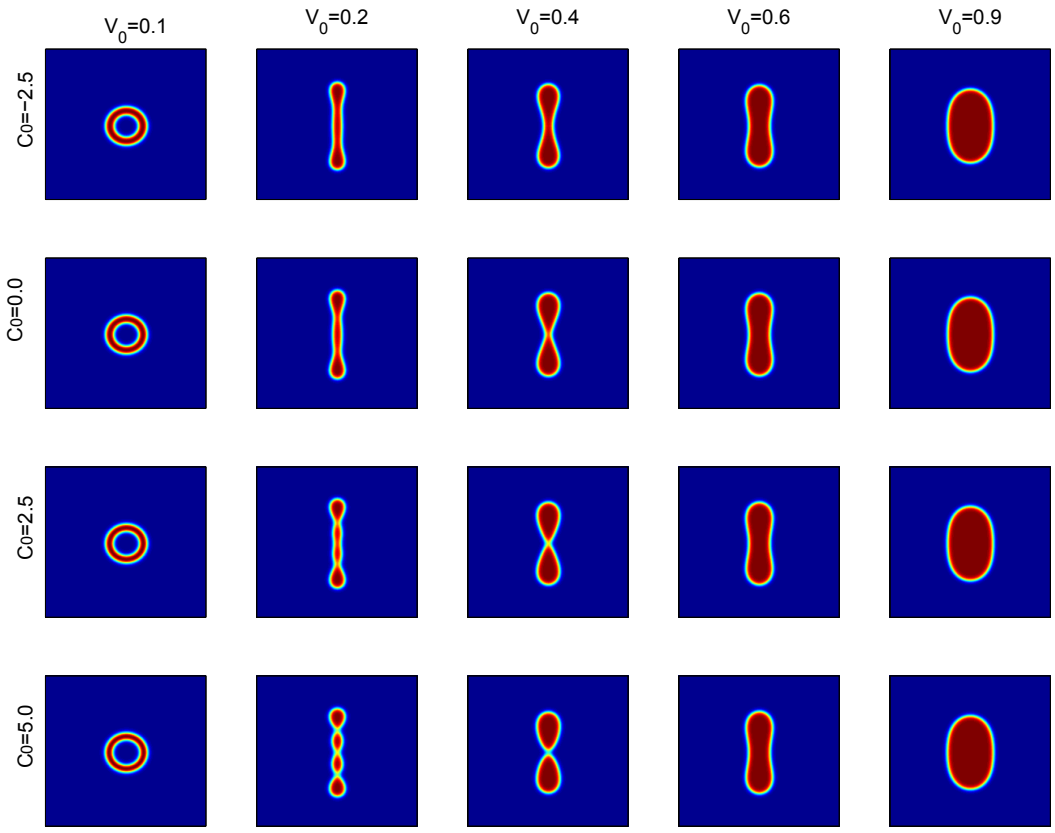

Figure 3.3: Different vesicle shapes controlled by the prescribed curvature c_0 and volume V_0.

Given different combinations of the prescribed volume and curvature, the vesicle may take different shapes. In Figure 3.3, for example, the cell transforms from the stomach shape to the prolate shape as the prescribed volume increases

when other conditions remain unchanged. Similar behavior has actually been observed in red blood cells [85].

3.4 Chemical reactions in a moving cell

A typical reaction diffusion equation usually takes the form

$$\frac{\partial A}{\partial t} = D\nabla^2 A + \mathrm{f}$$

where D is the diffusion coefficient, and f is the reaction function. The phase field implementation of the above equation is

$$\frac{\partial}{\partial t}(\phi A) = D\nabla \cdot (\phi \nabla A) + \phi \mathrm{f}$$

It has been proved that the boundary condition that no flux traverses across the membrane is satisfied [49]:

$$D\frac{\partial A}{\partial n}|_{a(t)} = -\frac{da}{dt}A + O(\epsilon)$$

Here a(t) is the moving boundary.

Since we consider actin flow in the cell later in Chapter 5, we further couple the reaction-diffusion equation to the flow field $\mathbf{u}$:

$$\frac{\partial}{\partial t}(\phi A) = -\nabla \cdot (\mathbf{u}\phi A) + D\nabla \cdot (\phi \nabla A) + \phi \mathrm{f}$$

3.5 Appendix

The explicit way to numerically solve differential equations is

$$\begin{aligned} \frac{dy}{dx} &= f(y,t) \\ y_{i+1} &= y_i + f(y_i, t_i)h, \end{aligned}$$

where h is the time step size, and i=0,1,. . . ,N is the step index.

An improved version is the adapted Euler method which is in fact a expectation-correction method

$$\begin{aligned} k_1 &= f(y_i, t_i)h \\ k_2 &= f(y_i + k_1, t_i + h)h \\ y_{i+1} &= y_i + \tfrac{1}{2}(k_1 + k_2) \end{aligned}$$

However, the explicit method requires small time steps. To keep it stable, the time step must satisfy

$$\Delta t < \frac{\Delta x^2}{2}.$$

As a result, explicit method usually consumes much computing time.

The implicit method is usually more stable than the explicit method,

$$y_{i+1} = y_i + f(y_{i+1}, t_{i+1})h.$$

Crank-Nicolson method is a combination of the explicit method and implicit method

$$y_{i+1} = y_i + \frac{f(y_i, t_i) + f(y_{i+1}, t_{i+1})}{2}h$$

It is unconditionally stable, but may leads to oscillations if time step is too large.

Both the implicit method and the Crank-Nicolson method are more difficult to implement than the explicit method because they require the inversion of matrix.

The equation describing the evolution of phase field reduces to a 4th order differential equation.

$$\frac{\partial \phi}{\partial t} + \nabla^4 \phi = F(\phi)$$

We employ the method in [98] and use the 2nd order backward differentiation formula. The time differential is

$$\frac{\partial \phi}{\partial t} = \frac{3\phi^{n+1} - 4\phi^n + \phi^{n-1}}{2\Delta t},$$

and hence

$$\frac{3\phi^{n+1} - 4\phi^n + \phi^{n-1}}{2\Delta t} + \nabla^4 \phi^{n+1} = F(\phi^{n+1}).$$

That is

$$(I + \frac{2}{3}\Delta t \nabla^4)\phi^{n+1} = \frac{4}{3}\phi^n - \frac{1}{3}\phi^{n-1} + \frac{2}{3}\Delta t F(\tilde{\phi}^{n+1}).$$

Note that $I + \frac{2}{3}\Delta t \nabla^4 = L_x L_y + \frac{4}{3}\Delta t \partial_{xxyy} - \frac{4}{9}\Delta t^2 \partial_{xxxx}\partial_{yyyy}$, where

$$L_x = I + \frac{2}{3}\Delta t \partial_{xxxx}, L_y = I + \frac{2}{3}\Delta t \partial_{yyyy}.$$

Therefore,

$$L_x L_y \phi^{n+1} = \frac{4}{3}\phi^n - \frac{1}{3}\phi^{n-1} - \frac{4}{3}\Delta t \partial_{xxyy}\tilde{\phi}^{n+1} + \frac{4}{9}\Delta t^2 \partial_{xxxx}\partial_{yyyy}\tilde{\phi}^{n+1} + \frac{2}{3}\Delta t F(\tilde{\phi}^{n+1})$$

Let $v = \phi^{n+1} - \tilde{\phi}^{n+1}$,

$$\begin{aligned} L_x q &= -\frac{2}{3}(\phi^n - \phi^{n-1}) - \frac{2}{3}\Delta t \nabla^4 \tilde{\phi}^{n+1} + \frac{2}{3}\Delta t F(\tilde{\phi}^{n+1}) \\ L_y v &= q \\ \phi^{n+1} &= \tilde{\phi}^{n+1} + v \end{aligned}$$

We further apply pseudo-linear factorization

$$\begin{aligned} L_x q &= -\frac{1}{3}(3\tilde{\phi}^{n+1} - 4\phi^n + \phi^{n-1}) - \frac{2}{3}\Delta t \nabla^4 \tilde{\phi}^{n+1} + \frac{2}{3}\Delta t F(\tilde{\phi}^{n+1}) \\ L_y v &= q \\ \phi^{n+1} &= \tilde{\phi}^{n+1} + v. \end{aligned}$$

$\tilde{u}^{n+1}$ is an estimate for u^{n+1} and is updated through multiple iterations. Let $\tilde{u}_0^{n+1} = 2u^n - u^{n-1}$, then for k=0, 1, ...

$$\tilde{u}_{k+1}^{n+1} = u_k^{n+1}$$

Note that L_x and L_y can be easily inverted through LU-decomposition.

Chapter 4

Computational model for cell morphodynamics

4.1 Introduction

Many eukaryotic cells can move using a crawling motion during which the front of the cell is extended by the polymerization of an actin filaments network. Forces applied to the substrate are mediated through adhesion and the detachment of the back of the cell is regulated by myosin and other proteins [63]. The modeling of this type of cell movement is a complex undertaking for several different reasons. First of all, the underlying signaling pathways responsible for controlling the movement are often poorly understood. For example, in eukaryotic chemotaxis, where cells are guided by chemical gradients, it is still unclear how cells determine their direction [42]. Furthermore, the forces that are generated during cell motion are most often not quantified, although recent experiments have started to address the cell-substrate interaction [21]. Lastly, cell movement is a dynamic process, involving cell membrane deformations and retractions that require a computational modeling strategy that can handle deformable boundaries. Not surprisingly, only a limited number of studies have attempted to address morphodynamics, the cell shape dynamics during movement (for a review, see [63]).

In this paper, we construct a quantitative model for cell shape dynamics

during motion based on the phase-field method. We apply it to the specific case of the motion of epithelial keratocytes. These cells extend a thin lamellipodium at the front and sides, with a bulbous cell body attached at the back [48]. Importantly, these cells can maintain rapid and persistent gliding motion over several cell lengths in the absence of external stimuli [27, 53, 95].

4.2 Model

We model the keratocyte as a two dimensional sheet with a fixed area A_0, although the extension to three dimensions is straightforward (albeit computationally expensive). The phase field takes on $\phi = 1$ in the interior of the cell and $\phi = 0$ represents the cell exterior. The shape of the cell membrane is determined by the interactions of various forces, including the surface tension, the bending force and the pressure that constrains the cell area, as in vesicles. We do not fix the cell perimeter, allowing the amount of membrane to change due to either the smoothing out of small-scale wrinkles or due to endo/exocytosis. We also consider the protrusion force from cross-linked actin filaments, the contraction force from the actin bundles and the effective friction due to cells' adhesion and attachment/detachment from the substrates.

The surface energy is proportional to the cell's perimeter L and can be implemented in the phase field formulations as [24, 57]

$$H_{ten} = \gamma L = \gamma \int (\frac{\epsilon}{2}|\nabla\phi|^2 + \frac{G}{\epsilon})d\mathbf{r},$$

where γ is the surface tension, ϵ is the parameter controlling the width of the cell boundary and where

$$G(\phi) = 18\phi^2(1-\phi)^2$$

is a double well potential with minima at $\phi = 0$ and $\phi = 1$. The area density of surface tension force is derived as follows:

$$\mathbf{F}^*_{ten} = -\frac{\delta H_{ten}}{\delta \mathbf{R}} = \frac{\delta H_{ten}}{\delta \phi}\nabla\phi = -\gamma(\epsilon\nabla^2\phi - \frac{G'}{\epsilon})\nabla\phi$$

This area density can be converted into a line density using

$$\mathbf{F}^*_{ten}d\mathbf{r} = \mathbf{F}_{ten}dl = \mathbf{F}_{ten}\epsilon|\nabla\phi|^2 d\mathbf{r}.$$

Thus

$$\mathbf{F}_{ten} = -\gamma(\nabla^2\phi - \frac{G'}{\epsilon^2})\frac{\nabla\phi}{|\nabla\phi|^2}.$$

This can also be seen by noting that the expression in brackets will vanish identically for thin planar interfaces if the phase field free energy

$$F[\phi] = \int \frac{1}{\epsilon}[\frac{(\epsilon|\nabla\phi|)^2}{2} + G]d\mathbf{r}$$

is minimized, and hence picks up its leading term from considering the expansion for a slightly curved thin interface with normal $\hat{n}$ and curvature c:

$$\nabla^2\phi \simeq (\hat{n}\cdot\nabla)^2\phi + c\hat{n}\cdot\nabla\phi.$$

Therefore, the tension force follows

$$\mathbf{F}_{ten} = -\gamma c\hat{n}.$$

This is consistent with the Young-Laplace equation, which states that the net component of the surface tension forces is normal to the surface and proportional to the local curvature.

Helfrich [40] modeled the bending energy as

$$H_{bend} = \frac{\kappa}{2}\oint c^2 dl$$

where κ is the bending rigidity and where l denotes the arclength along the perimeter. This term can be implemented as [24, 57]

$$H_{bend} = \frac{\kappa}{2}\int \frac{1}{\epsilon}[\epsilon\nabla^2\phi - \frac{1}{\epsilon}G']^2 d\mathbf{r}$$

Note that we have taken the spontaneous curvature to be 0. We then derive the bending force's area density and convert it into a line density as above:

$$\mathbf{F}_{bend} = \kappa(\nabla^2 - \frac{G''}{\epsilon^2})(\nabla^2\phi - \frac{G'}{\epsilon^2})\frac{\nabla\phi}{|\nabla\phi|^2}$$

We have verified that this expression is identical to the one employed by Biben and Misbah [9].

Experiments show that the cell area $A = \int \phi d\mathbf{r}$ is conserved during deformation and movement [48]; the same study indicates that perimeter is not highly conserved. Thus we introduce a constraint term:

$$\mathbf{F}_{area} = -M_A(A - A_0)\hat{n} = M_A(\int \phi d\mathbf{r} - A_0)\frac{\nabla\phi}{|\nabla\phi|}$$

where M_A is large and where A_0 is the prescribed area.

The coupling of the actin-myosin system provides a differential extension / retraction force for the cell membrane and thus generates the cell's movement. Specifically, at the leading edge of the cell, the actin filaments form a highly cross-linked network and the polymerization of actin filaments pushes the cell membrane forward. At the back of the cell actin filaments reorganize and align into bundles which, with the help of the molecular motor myosin-II, generate retraction forces [52, 65]. Despite intensive studies on the actin-myosin system, the detailed mechanisms underlying this system are still quantitatively uncertain. We will therefore proceed phenomenologically and assume that the protrusion and retraction force is simply proportional to the concentration of cross-linked actin filaments, denoted by V, and the concentration of actin bundles, denoted by W:

$$\mathbf{F}_{prot} = \alpha V\hat{n} = -\alpha V\frac{\nabla\phi}{|\nabla\phi|}; \mathbf{F}_{retr} = -\beta W\hat{n} = \beta W\frac{\nabla\phi}{|\nabla\phi|}$$

where α and β are coefficients that determine the magnitude of the protrusion and retraction forces. The cross-linked actin filaments grow at a constant rate a while both filaments and bundles depolarize with rates c and e, respectively, and diffuse inside the cell [95]. Furthermore, some of the filaments align parallel to each other and form actin bundles and we assume that preexisting actin bundles help this alignment of actin filaments, leading to a non-linear coupling term. The resulting dynamical equations for V and W can be coupled to the phase field in a consistent way [49]:

$$\begin{aligned}\frac{\partial(\phi V)}{\partial t} &= \phi(a - bVW^2 - cV) + D_V\nabla\cdot(\phi\nabla V)\\ \frac{\partial(\phi W)}{\partial t} &= \phi(bVW^2 - eW) + D_W\nabla\cdot(\phi\nabla W)\end{aligned}$$

Note that the inclusion of these forces extends work by others [57, 8, 24, 11] who focused on vesicles. Our model does not include, however, a coupling to the

dynamics of the surrounding fluid as in recent work by Misbah and collaborators [8].

When keratocytes slide over the substrate, the adhesiveness between the cells and substrate, along with the attachment and detachment of cells from the substrate can be viewed as an effective friction that is proportional to the local speed [51]:

$$\mathbf{F}_{fr} = -\tau \mathbf{v}.$$

At quasi-steady state (neglecting inertia), the total force is approximately zero

$$\mathbf{F}_{tot} = \mathbf{F}_{ten} + \mathbf{F}_{bend} + \mathbf{F}_{area} + \mathbf{F}_{prot} + \mathbf{F}_{retr} + \mathbf{F}_{fr} = 0$$

and since the evolution of phase field ϕ follows

$$\frac{\partial \phi}{\partial t} = -\mathbf{v} \cdot \nabla \phi,$$

we get the final equation for ϕ:

$$\begin{aligned} \tau \frac{\partial \phi}{\partial t} &= -\kappa(\nabla^2 - \frac{G''}{\epsilon^2})(\nabla^2 \phi - \frac{G'}{\epsilon^2}) + \gamma(\nabla^2 \phi - \frac{G'}{\epsilon^2}) \\ &\quad -M_A(\int \phi d\mathbf{r} - A_0)|\nabla \phi| + (\alpha V - \beta W)|\nabla \phi| \end{aligned}$$

Physically, this means that the friction force on the cell is balanced by the active protrusion and retraction forces, which are transmitted from the substrate onto the cell via adhesion complexes [31]. Thus, the total force from the substrate onto the cell vanishes, as can be explicitly checked for our computed solutions. In our model, as in real locomoting objects, the action of the active elements are not merely internal, but instead are coupled to the external surroundings (here the substrate) and can cause non-zero momentum transfer.

This fourth order nonlinear partial differential equation was solved using an alternating direction implicit scheme and a second order backward differentiation formula.

4.3 Computational method

We used a 600×200 rectangular grid with grid size of 0.1 μm and time step of $\Delta t = 10^{-4} s$. To cut the computing time, we move the computational box with

Table 4.1: Model parameters on cell morphodynamics

	Description	Value
γ	surface tension	1.0 pN
κ	bending rigidity	1.0 pNμm^2
α	coefficient of F-actin extension	0.1 $pN/\mu m$
β	coefficient of myosinII retraction	0.2 $pN/\mu m$
M_A	area constraint	1.0 $pN/\mu m^3$
A_0	prescribed area	50.24 μm^2
ϵ	3 times boundary width	1.0 μm
τ	friction coefficient	2.62 $pNs/\mu m^2$
a	actin filament growth rate	$0.084s^{-1}$
b	actin filaments transform to bundles	$1.146s^{-1}$
c	filament depolarization rate	$0.0764s^{-1}$
e	bundle depolarization rate	$0.107s^{-1}$
D_V	diffusion coefficient of actin filaments	$0.382\mu m^2/s$
D_W	diffusion coefficient of actin bundles	$0.0764\mu m^2/s$

the cell's centroid such that the boundary of this box is at least 25 grids points away from the cell membrane. We have verified that taking a larger computational box does not change the quantitative results. To further reduce the computational costs, we have parallelized the algorithm and the final code required approximately 4 hours on 4 CPUs for 200 s, which was long enough to reach a steady state.

4.4 Results

Our two-dimensional simulation parameters are obtained from measured three dimensional values by assuming a cell height of $0.1\mu m$. For example, the surface tension parameter in the simulations is derived from the measured value γ_{exp} by the conversion $\gamma = 0.1\mu m \cdot \gamma_{exp}$. Experimental values for this parameter and for the bending rigidity are, to our knowledge, not available for keratocytes and we have taken values reported by shear flow experiments using *Dictyostelium* cells [88]: $\gamma_{exp} \sim 10pN/\mu m$ and $\kappa_{exp} \sim 10pN\mu m$. Note that the surface tension value is much lower than the values reported using micropipette aspiration [19, 78] and that this discrepancy has been attributed to the role of the cytoskeleton [61]. Indeed, results obtained [109] using micropipette aspiration for cells in which actin

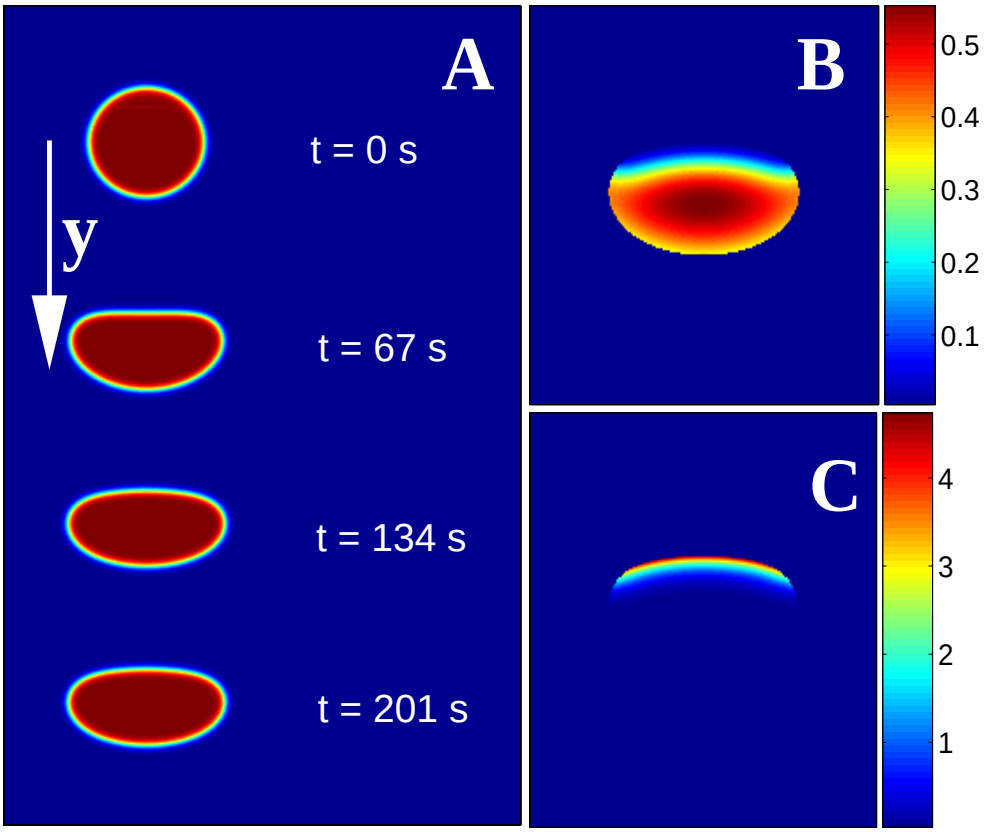

Figure 4.1: (A) Snapshots of the numerical evolution of a cell shape. The phase field is shown in a color scale with the interior of the cell ($\phi = 1$) plotted as red and the exterior of the cell ($\phi = 0$) plotted in blue. The resulting distributions of V and W are shown in B and C, respectively.

polymerization has been abolished give values that are close to the one reported in Ref. [88]. Other values of the simulation parameters can be found in Table 1 and it is important to note that we can obtain similar qualitative results for a wide range of parameters.

A typical simulation started with a circular stationary cell with radius $r_0 = 4.0\mu m$, V=1.1 and W=0 uniformly. Since our reaction-diffusion system is linearly stable, we break the symmetry by assigning a spatially varying concentration field for W. For example, we can take $W = W_0 y$ for $y < 0$ and $W = 0$ otherwise, where **y** is a randomly chosen direction and y=0 is at the cell's center. Simulations show that different asymmetric initial conditions lead to the same steady state. Due to

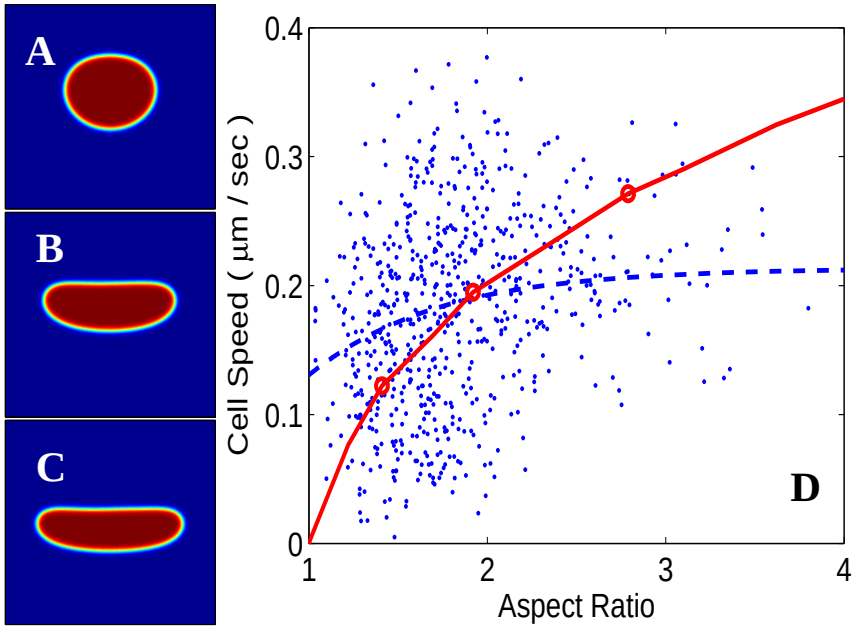

Figure 4.2: Snapshots of three steady state solutions of our model for $a = 0.069s^{-1}$ (A), $a = 0.084s^{-1}$ (B) and $a = 0.107s^{-1}$ (C). The corresponding aspect ratios and cell speeds are $S = 1.41$ and $v = 0.12\mu m/s$, $S = 1.92$ and $v = 0.19\mu m/s$, and $S = 2.79$ and $v = 0.27\mu m/s$. (D) Cell speed as a function of the aspect ratio. The solid line is our simulation result, the dots are experimental results from [48] and the dashed curve is the prediction from the simple model in [48]. The three circles correspond to A, B, and C.

the asymmetric distribution of W, the cell will retract from the edge with highest W and will start to move. As the cell moves forward, actin bundles are sequestered at the rear and its concentration is increased through the positive feedback loop while the cell's leading edge is characterized by a high concentration of cross linked actin filaments. A final steady state is reached when the cell has a stationary shape with a constant speed and stationary distributions of V and W. An example is shown in Figure 4.1A for the particular set of parameter values of Table 1. The cell's area changed by less than 0.1% throughout the process. Figgure 4.1B and C show the steady state distribution of V and W.

To obtain different cell shapes and speeds we changed the value of growth rate a. The different cell shapes can be quantified by the aspect ratio S, defined as the ratio of the cell width and the cell length. When the growth rate a is small,

the amount of V and W is limited and the cell has little asymmetry. Therefore, the cell is nearly circular and moves slowly. Increasing the value of a corresponds to increasing the amount of both filaments network and bundle, providing larger driving forces for cell movement, and hence increases the cell's speed and aspect ratio. In Figure 4.2A-C we plot the steady state solution of several cells with increasing speeds and aspect ratios.

Due to the coupling between the V and W field and the corresponding protrusion and retraction forces, there is a monotone relationship between the aspect ratio and the speed of the cell: the cell moves faster for larger aspect ratios. This is shown in Figure 4.2D where we plot the speed as a function of the aspect ratio in our simulations (solid line). The cells shown in Figure 4.2A-C correspond to the circles. As a comparison, we have also plotted the experimental results (dots) and the prediction of a simple model (dashed line) from Ref. [48]. This simple model does not compute the actual cell shape or the cell dynamics and determines the cell's speed based solely on the actin distribution. This is in contrast to our model, which explicitly provides the shape of the cell and requires a retraction mechanism, provided here by the W field. Furthermore, our simulation results, unlike the simple model, predict a zero velocity for $S = 1$. This corresponds to the case where the cross linked actin filaments and bundles concentration is distributed uniformly in the cell. Thus, there is no asymmetry and the cell will not move. To fit the results of our method we simply varied the friction coefficient and found that the value of τ given in the table gave the best fit to the experimental data. Clearly, the experimental data exhibits a large amount of variability, precluding a comparative quantitative analysis of the fits provided by the two models. Further progress would therefore depend on reducing this variability (if possible) by more tight protocols or on extending the model to allow for some degree of cell-to-cell parameter variability.

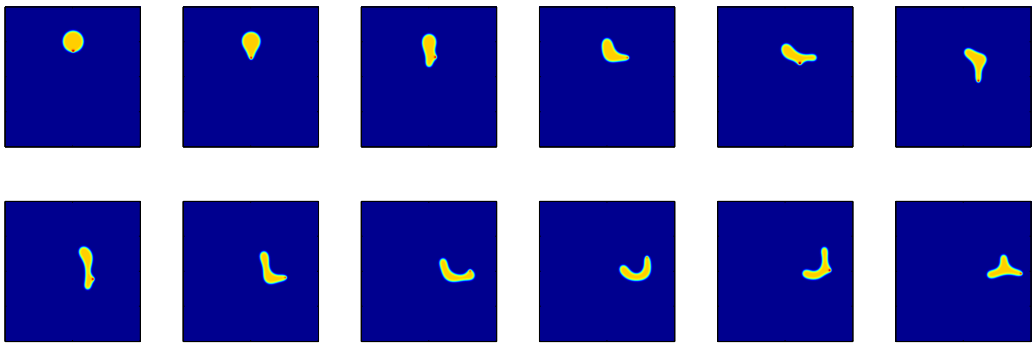

Figure 4.3: Simulated crawling of the *Dictyostelium* cell.

4.5 Application to *Dictyostelium* cells

Dictyostelium cells are quite different from Keratocyte cells. They can sense chemoattractant, organize patches and extend pseudopods to find the way forwards. Suppose that the chemoattractant concentration increase from top to bottom and the cell can amplify the external gradient to a step function through certain signaling pathways. We started with a rounded cell with one patch at the bottom (Figure 4.3). The patch (labeled in red spot) was replaced every one minute at a random place at the front half of the cell. Our simulation shows that although the cell does not go straightly downwards, it gradually descends.

4.6 Discussion

In summary, we have presented a phase field description of motile cell shapes. This method has a main advantage that it is able to find cell shapes without the need for an explicit boundary tracking algorithm. The development of this method puts us in an excellent position to start addressing the coupling between intra-cellular dynamics and cell motion. A framework of the type proposed here is a necessary prerequisite for this future investigation. Finally, we are currently investigating the application of our ideas to other cell types in general,

and chemotaxing cells in particular. There, the cells receive external signals that are translated into internal chemical cues [50, 55]. Formulating models in which these internal cues generate significant cell deformations has been proved to be challenging [105]. Indeed, the coupling of models describing the internal pathways with cell motion is a difficult task, but one for which our method should be well suited.

4.7 Acknowledgments

This work was supported by NIH Grant P01 GM078586. We thank Zachary Pincus and Alex Mogilner for providing us the experimental data.

This chapter is based on the following published paper:

D. Shao, W.J. Rappel and H. Levine. Computational model for cell morphodynamics, *Phys. Rev. Lett.*, 105, pages 108104–108107.

Chapter 5

Coupling actin flow and adhesion mechanism during cell migration

5.1 Introduction

In many eukaryotic cells, the migration is powered by the actin-myosin system [72] and assisted by the adhesion between cells and substrates [31]. At the cell's leading edge, the cross-linked actin filaments polymerize by adding actin monomers to their barbed ends, a process known as "tread-milling"; while at the back of the cell, myosin II binds to the bundled actin filaments and exerts contractile stress.

The active stresses generated by the actin-myosin system are transmitted to the substrates through adhesion sites [31, 34, 44]. Nascent adhesion sites are formed near the front of the cell, grow into focal adhesions and gradually dissemble as the cell advances [1, 16, 34]. Many studies have indicated that the forces exerted by the adhesion sites could be in two different modes. One is called the gripping mode, where the adhesion sites act like engaged clutches and link the actin network tightly to the substrates. When the clutch is disengaged, the adhesion site transformed into the slipping mode, exerting frictional drag [13, 45]. More recently, Verkhovsky's group analyzed the relationship between actin flow and substrate stress[31]. They found that the substrate stress was not always aligned with the

actin flow and the magnitude of the stress did not follow that of the flow velocity monotonically, indicating that slipping mode alone was insufficient to explain the adhesion mechanism.

Recent experiments have examined the movement of actin network with

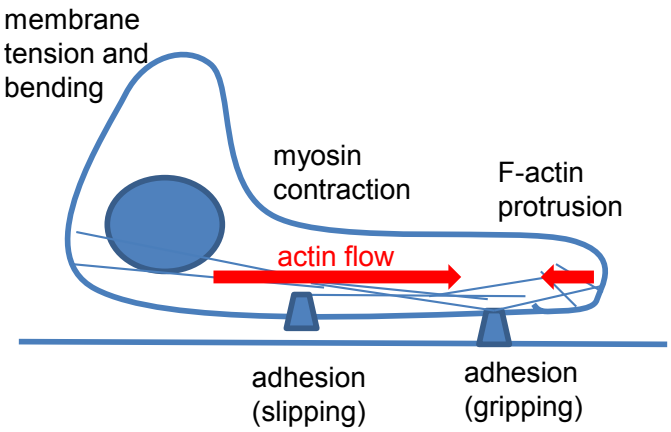

Figure 5.1: Schematic diagram of the migration model.

Cell migration has been modeled from various perspectives. On the whole cell level, some pioneer works modeled the actin network as a strip of gel using Kelvin-Voight model and obtained one dimensional map of actin flow [37, 51]. Rubinstein *et al.* studied the viscoelastic flow in a presumed 2D cell geometry [79]. In later studies, the cell periphery was updated according to a phenomenal function of protrusion rate [3, 99]. Our previous phase field model implemented physical forces along the cell membrane and obtained cell shape and speed by [86]. More recently, Carlsson *et al.* treated the actin polymerization as an active

stress. Contrary to the contractile stress caused by myosin II, actin polymerization generates expansive stress. He further analyzed how the distribution of active stresses and adhesion strength contribute to cell motility in 1D [12]. However, all the above works modeled adhesion as pure frictional drag, and didn't consider the gripping mode of adhesion sites. Also, they ignored the dynamics of adhesion sites. Aside from the whole cell models, adhesion dynamics and its gripping effect were studied in isolated context [10, 13, 17].

We built a comprehensive model on cell migration. The moving boundary of the cell was solved by the phase field method. In the model, both myosin II contraction and actin polymerization were treated as active stress as in [12]. Moreover, the adhesion sites could switch between the gripping mode and the slipping mode, and their dynamics were integrated with actin flow. We also included tension forces and bending forces at the membrane. The model explained the decoupling of actin flow direction and substrate stress direction in the central part of the cell. Furthermore, we explored the collective effect of myosin II and gripping strength on cell motility and cell shape.

5.2 Model

The model system is the Keratocyte cell, which extends broad Lamellipodia and has a stereotyped fan-like shape. The cell body is ignored in our model since it's been reported that lamellar fragments alone can retain the fan-like shape and motility [96]. Because the lamellipodia is rather flat, we modeled in two dimensions. Note that extension to three dimensions is straight forward but much more intensive in computation. The model is illustrated in Figure 5.1. The actin network is treated as viscoelastic fluid [79]. At quasi steady state,

$$\upsilon_0 \nabla \cdot [\phi(\nabla \mathbf{u} + \nabla \mathbf{u}^T)] + \nabla \cdot \sigma_{\text{myo}} + \nabla \cdot \sigma_{\text{poly}} + \mathbf{F}_{\text{adh}} + \mathbf{F}_{\text{mem}} = \mathbf{0}$$

In the first term, the symmetrized strain rate tensor

$$\nabla \mathbf{u} + \nabla \mathbf{u}^T$$

is coupled with the phase field ϕ, where $\mathbf{u}$ denotes the velocity of actin flow. υ_0 is the effective viscosity of actin network. The phase field can be viewed as an indication of cell territory since it is constructed such that $\phi = 1$ inside the cell and $\phi = 0$ outside the cell [8, 86]. The next two terms describe the active stresses coming from myosin II and actin filaments respectively. Myosin II that is bounded to the bundled actin network can generate contractile stress. We assume that the contractile stress is isotropic and its magnitude is proportional to the myosin II density ρ_m, and thus

$$\sigma_{\text{myo}} = \eta_m^0 \phi \rho_m \mathbf{I}.$$

Meanwhile, the polymerization of actin filaments generates expansive stress [12]. The expansive stress is probably confined to the cell periphery because the actin filaments are oriented in such a way that their barbed ends, where the new actin monomers are added, are close to the cell membrane and point outwards [72]. We assume that the stress is normal to the membrane and increases linearly with the cross linked F-actin density ρ_a. Let $\hat{n}$ and $\hat{t}$ be normal vector and tangential vector with respect to cell boundary respectively. Under the coordinate system ($\hat{n}$, $\hat{t}$),

$$\sigma_{\text{poly}} = -\eta_a^0 \phi \rho_a \delta_\epsilon \begin{pmatrix} 1 & 0 \\ 0 & 0 \end{pmatrix}$$

When transformed to the ($\hat{x}$, $\hat{y}$) coordinate system, it comes

$$\sigma_{\text{poly}} = -\eta_a^0 \phi \rho_a \delta_\epsilon \begin{pmatrix} \hat{x}^2 & \hat{x}\hat{y} \\ \hat{x}\hat{y} & \hat{y}^2 \end{pmatrix}$$

Here, $\delta_\epsilon = \epsilon(\nabla\phi)^2$ labels the cell periphery, where ϵ is the characteristic width of the phase field boundary.

Many studies have shown that the adhesion mechanism is more complex than frictional drag and an intriguing solution is to treat the adhesion sites as clutches [31, 45]. When the clutches are engaged, the adhesion sites are in the gripping mode; and once disengaged, the adhesion sites switch to the slipping mode. Moreover, evidences have shown that the adhesion sites are formed at the front part of cell and nascent focal adhesions generate stronger propulsive forces [1, 5]. Therefore, we modeled the adhesion part in the following way. Assume that

there is always a small friction between the cell and the substrate with uniform coefficient ξ. On top of that, each adhesion site is born in the gripping mode at a random birthplace. The birthplace has a probability distribution density proportional to the density of cross-linked actin filaments ρ_a, so that the nascent adhesion sites concentrate at the front of the cell as ρ_a does. The gripping mode is modeled as a spring with two ends. One end (with position $\mathbf{x_0}$) grips the substrate, and doesn't move. The other end (with position $\mathbf{x}$) is connected to the actin network, and thus travels with the actin flow at velocity $\mathbf{u}$. The initial spring length is set to zero. As the spring is stretched, it will exert an elastic force

$$\mathbf{F}_{\text{grip}} = -k_{\text{grip}}(\mathbf{x} - \mathbf{x_0}),$$

where k_{grip} is the spring coefficient. The spring might break according to Bell's law

$$r_{\text{off}} \sim \exp(|\mathbf{F}_{\text{grip}}|/F_0),$$

where the breaking rate r_{off} increases exponentially with the gripping force [10, 13]. Once the spring breaks, the end attached to the substrate is retreated and the adhesion site switches to the slipping mode. The adhesion site now exerts frictional force

$$\mathbf{F}_{\text{slip}} = -k_{\text{slip}}\mathbf{u}.$$

Because the adhesion sites are growing [34] and larger substrate stress was observed at the sides of the cell [31], we assume that both gripping coefficient k_{grip} and slipping coefficient k_{slip} increase linearly with the age of the adhesion site t_{adh}, that is

$$k_{\text{grip}} = k^0_{\text{grip}} t_{\text{adh}}$$

and

$$k_{\text{slip}} = k^0_{\text{slip}} t_{\text{adh}}.$$

The slipping site can go back to gripping mode with rate r_{on} or die with rate r_{die} ($r_{\text{on}} \ll r_{\text{die}}$). Additionally, the adhesion site is forced to die once it hits the cell boundary ($\phi > 0.5$). The dead site is reborn immediately and enters the next cycle, such that the total amount of adhesion sites is fixed.

The membrane forces, including tension force and bending force

$$\mathbf{F}_{\text{mem}} = \mathbf{F}_{\text{tension}} + \mathbf{F}_{\text{bend}},$$

can be formulated in the phase field framework [24, 86]:

$$\mathbf{F}_{\text{tension}} = -\gamma(\epsilon\nabla^2\phi - \frac{G'}{\epsilon})\nabla\phi,$$

$$\mathbf{F}_{\text{bend}} = \kappa\epsilon(\nabla^2 - \frac{G''}{\epsilon^2})(\nabla^2\phi - \frac{G'}{\epsilon^2})\nabla\phi.$$

Here, $G = 18\phi^2(1-\phi)^2$ is the double well potential for the phase field.

It's commonly accepted that the cross linked actin filaments occupy the leading edge while myosin II is more concentrated near the tail during cell migration [96]. To polarize the cell, we use a mass conserved reaction to describe the kinetics of ρ_a [68, 66],

$$f(\rho_a, \rho_a^{\text{cyt}}) = k_b(\frac{\rho_a^2}{K_a^2 + \rho_a^2} + k_a)\rho_a^{\text{cyt}} - k_c\rho_a$$

The first term on the right hand side is the rate of polymerization which depends on the cytosolic concentration of actin monomers ρ_a^{cyt}. Since the actin monomers are small molecules and can diffuse fast, we assume that they are uniformly distributed in the cell and thus

$$\rho_a^{\text{cyt}} = (\rho_a^{\text{tot}} - \int \rho_a \mathbf{dx})/A,$$

where A is the total area of the cell. The second order Hill function accounts for possible positive feedbacks in the polymerization process. The last term is a simple depolymerization rate. We then couple the reaction to the convection of actin network and added a slow diffusion. The phase field implementation is [49, 86]:

$$\frac{\partial}{\partial t}(\phi\rho_a) = -\nabla\cdot(\phi\rho_a\mathbf{u}) + D_a\nabla\cdot(\phi\nabla\rho_a) + \phi f(\rho_a, \rho_a^{\text{cyt}})$$

Note that the reaction of ρ_a is independent of ρ_m here. Some studies have shown that the myosin II is not indispensable in cell migration and cells treated with myosin II inhibitor can still maintain their polarized shape and move forward [31, 45].

The bounded myosin II travels with the actin flow [84] and diffuses with coefficient D_m,

$$\frac{\partial}{\partial t}(\phi\rho_m) = -\nabla\cdot(\phi\rho_m\mathbf{u}) + D_m\nabla\cdot(\phi\nabla\rho_m)$$

Because the actin flow is slower than the cell speed at most part of the cell, or even retrograde in the leading edge, the bound myosin II, which travels with the actin flow, falls behind and is sequestered near the cell back. To further prevent myosin II from diffusing into the leading edge, we assume that the diffusion of myosin II is reduced when the density of cross linked actin network is high

$$D_m = \frac{D_m^0}{1 + \rho_a / K_D}.$$

Finally, we assume that the cell periphery should move at the same velocity as the local velocity of actin flow, and update the phase field ϕ accordingly,

$$\frac{\partial \phi}{\partial t} = -\mathbf{u} \cdot \nabla \phi + \Gamma(\epsilon \nabla^2 \phi - \frac{G'}{\epsilon} + c\epsilon |\nabla \phi|)$$

Note that the last term is added to stabilize the phase field interface, where c denotes the local curvature

$$c = \nabla \cdot \hat{n} = -\nabla \cdot \frac{\nabla \phi}{|\nabla \phi|},$$

and Γ is a Lagrangian multiplier [8].

The partial differential equations are computed on a 800×200 rectangle with grid size of $0.2\mu m$ and time step $\Delta t = 10^{-4} s$. The force generated by each adhesion site is distributed equally to the nearest four grids that encloses the site. To reduce the computing time, we define a computation box that encloses the cell such that the boundary of the cell is at least 18 grids away from the sides of the box. The actin flow equation is solved by implicit scheme and the reaction diffusion equations are calculated explicitly at locations where $\phi > 10^{-4}$. The parameters are provided in Table 1.

5.3 Results

The simulation starts from a discoid cell with radius $r_0 = 10\mu m$. Initially, the myosin II is uniformly distributed with density $[\rho_m^0]$; while the cross linked actin filaments only occupy the front half of the cell. The polymerization of actin filaments pushes the cell forward and myosin II falls behind. As the myosin II

Table 5.1: Model parameters on cell migration

	Description	Value
υ_0	effective viscosity of actin flow	10^3pN·s/μm
η_m^0	myosinII contraction coefficient	100pN $\cdot$ μm
η_a^0	F-actin protrusion coefficient	560pN $\cdot$ μm^2
F_{grip}^0	characteristic gripping stress	$0.1 \sim 10$Pa
k_{grip}^0	gripping coefficient	2.5Pa/(s·μm)
k_{slip}^0	slipping coefficient	0.25Pa/μm
ξ	base friction coefficient	0.5Pa·s/μm
r_{on}	slipping to gripping rate	$0.005s^{-1}$
r_{off}	gripping to slipping	$0.002s^{-1}$
r_{die}	death rate of slipping site	$0.2s^{-1}$
k_a	base polymerization rate	0.01
k_b	F-actin polymerization rate	$10s^{-1}$
K_a	positive feedback threshold	$1\mu m^{-2}$
k_c	F-actin depolymerization rate	$10s^{-1}$
D_a	actin network diffusion coefficient	$0.8\mu m^2/s$
D_m^0	max myosin diffusion coefficient	$2\mu m^2/s$
K_D	myosin diffusion threshold	$2\mu m^{-2}$
γ	tension coefficient	20pN
κ	bending coefficient	20pN $\cdot$ μm^2
ρ_a^{tot}	total amount of actin	800
$[\rho_m^0]$	initial density of myosin II	$0.2 \sim 0.4\mu$m^{-2}
N_{adh}	number of adhesion sites	1000
ϵ	width of phase field	$2\mu m$
Γ	lagrangian multiplier	$0.4\mu m/s$

gathers at the back of the cell, it produces contractile stress and retract the cell rear. During the migration, the cell evolves and finally reaches a stationary fan-like shape (Figure 5.2A) and a constant speed. Figure 5.2B and Figure 5.2C show the steady state distribution of cross linked actin filaments and bounded myosinII respectively.

5.3.1 Coupling of actin flow and stress

The map of the actin flow predicted by our model is shown in Figure 5.3A and the y-direction actin velocity along the midline is plotted in Figure 5.3D for

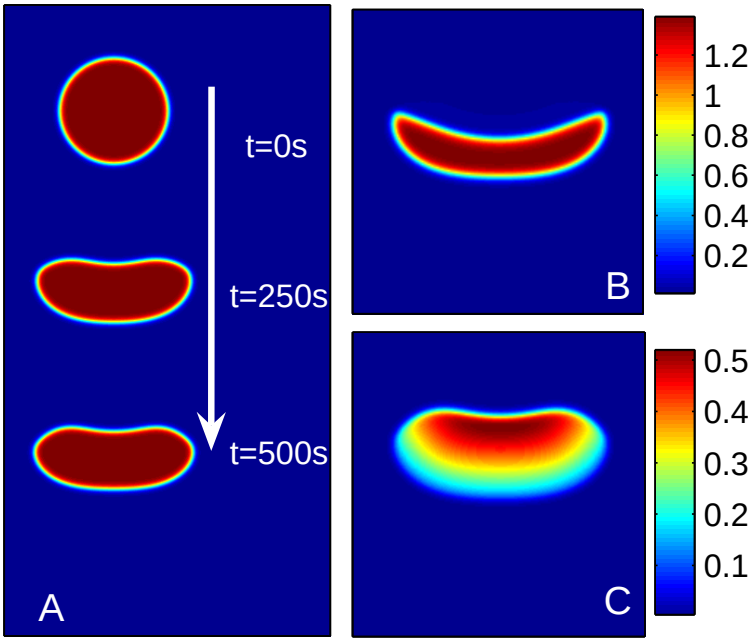

Figure 5.2: The snapshots of cell migration. (A) The cell evolves and reaches a stationary shape with aspect ratio $S = 2.6$ and speed $v = 0.14\mu m/s$. (B) and (C) The steady-state distributions of F-actin (B) and bounded myosinII (C). Here, $F^0_{\text{grip}} = 5$ Pa and $[\rho^0_m]$=0.3 μm^{-2}.

better visualization. The actin network flows forward in most part of the cell with increasing speed towards the back and the sides. However, the leading edge of the cell is characterized by a retrograde flow with a small backwards velocity of $\sim 0.012\mu$m/s. The retrograde flow is induced by myosin II contraction, the actin polymerization and the membrane tension collectively. The sharp spike ahead of the retrograde represents the forward movement of the cell boundary, which is pushed by the polymerization of actin filaments. At steady state, the front and the back boundaries move with the same velocity $v_{\text{front}} = v_{\text{back}} = v_{\text{cell}} = 0.14\mu$m/s. The whole picture is consistent with previous experimental observations [45, 31]. It can be seen from figure 5.3D that the divide between the retrograde flow and the anterograde flow has been shifted toward the leading edge. This is due to the strong gripping stress exerted by the adhesion sites near the cell front.

Figure 5.3B illustrates the predicted substrate stress, which includes the basel level friction between the cell and the substrate, the added friction from slipping sites and the spring stress from gripping sites. we have checked that the substrate stress sums up to zero at steady state. Note that the strongest stress lies at the flanks of the cell as is observed in the experiment [31]. One reason is that the actin flow here is fast. Moreover, the strength of the adhesion sites increases as they grow [34]. Most adhesion sites start their journey from the leading edge. When they reach the flanks of the cell, they have grown up and can exert stronger stress. The stress drops near the trailing part of the cell simply because many adhesion sites have died off before reaching here.

We further investigated the alignment between actin flow and substrate stress. Let θ be the angle between the vector of actin flow and the vector of substrate stress. The image of $\cos\theta$ is shown in Figure 5.3C, and is in perfect agreement with the experimental observation [31]. If the adhesion mechanism were purely frictional drag, the substrate stress would be in the same direction as the actin flow, that is $\theta = 0$ and $\cos\theta = 1$ (red color). However, at the central part of the cell, the substrate stress is not perfectly aligned with the actin flow ($\cos\theta < 1$), or even opposite to the actin flow ($\cos\theta = -1$), indicating that the slipping mode alone can not explain the whole picture. To reproduce the $\cos\theta < 1$

region, we implemented an extra gripping mode with an elastic spring. The stress no longer correlates with the flow velocity, but instead depends on the cumulated stretch of the spring. For example, a gripping site is created at the leading edge with retrograde flow. The sprint end bound to the actin network moves backwards and thus the substrate feels a backwards stress. In the next moment, the actin flow might switch its direction and moves forward, while the string is still stretched backwards, resulting in the opposite alignment of actin flow and substrate stress and $\cos\theta = -1$.

Figure 5.3E and F illustrate the distributions of gripping sites and slipping sites respectively. The gripping sites concentrate in the front of the cell while slipping sites are populated at the sides and back.

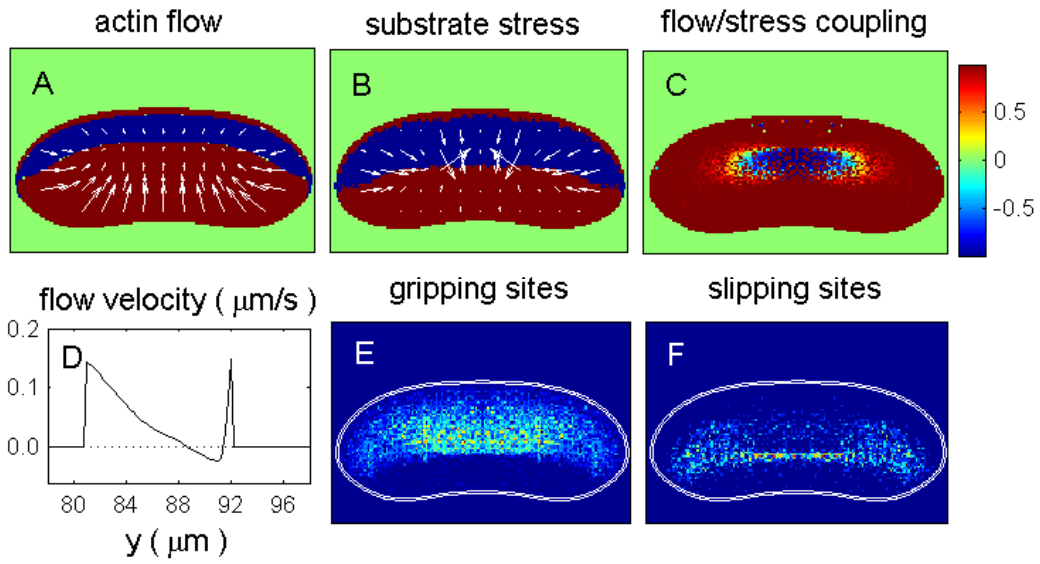

Figure 5.3: Comparative maps of actin flow and substrate stress. (A) The map of actin flow. (B) The map of substrate stress. (C) The alignment of actin flow and substrate stress, which is measured by the cosine of the angle between flow vector and stress vector. (D) Actin flow along the y direction at the middle of the cell as is indicated in (A). (E) Distribution of gripping sites. (F) Distribution of slipping sites.

5.3.2 Both myosin II and gripping strength effect cell velocity and cell shape

To explore the cell motility under different conditions, we varied myosin II level and the strength of gripping sites (Figure 5.4). Initially, the cell velocity increases with gripping strength (Figure 5.4A), because the gripping sites anchor the actin network to the substrate, stall the retrograde flow (Figure 5.4B) and help to pull the cell back forward (Figure 5.4C). However, once the gripping stress becomes too strong, it reduces the anterograde flow and hinders the forward crawling of the cell.

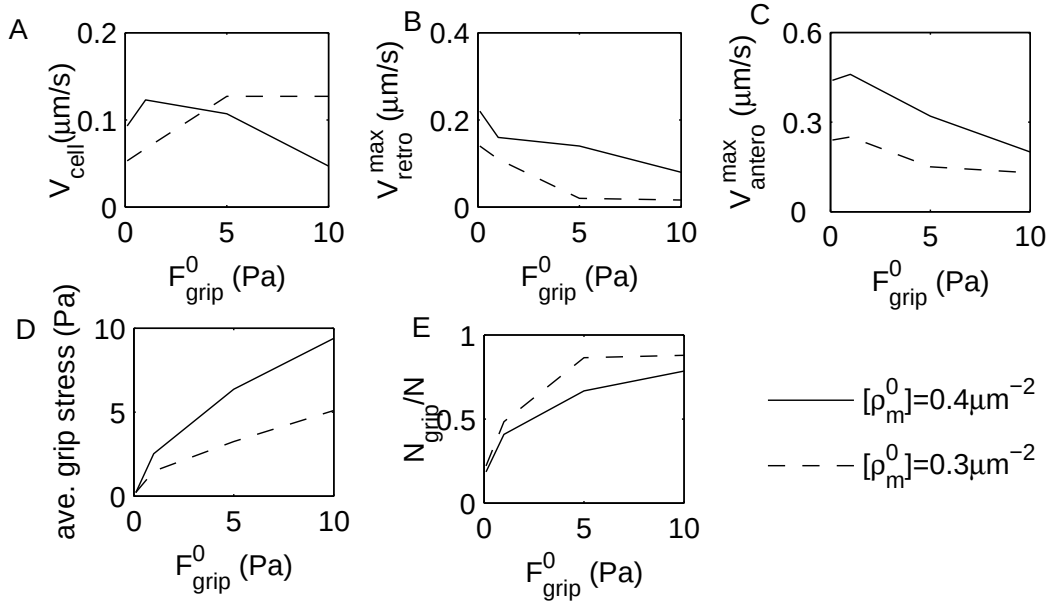

Figure 5.4: Cell velocity is effected by both myosin II and gripping strength. (A) Cell velocity. (B) and (C) Take the y-direction actin flow along the midline of the cell and plot the maximum speed of retrograde flow (B) and the maximum speed of anterograde flow (C). (D) The average gripping stress. (E) The percentage of the adhesion sites that are in the gripping mode. Solid line represents $[\rho^0_m] = 0.4\mu\text{m}^{-2}$ and dashed line $[\rho^0_m] = 0.3\mu\text{m}^{-2}$.

Decreasing the level of myosin II will reduce both the retrograde flow and anterograde flow (Figure 5.4B and C). This is consistent with the experimental results that cells treated with blebbistatin (a myosin II inhibitor) have slower

inward flow [97, 3]. However, the effect of myosin II contraction on cell velocity is biphasic (Figure 5.4A). On one hand, higher level of myosin II, which generates larger contractile stress, can expedite cell migration, as was analytically proved in [12]. On the other hand, higher contractile stress requires stronger gripping stress to anchor the cell's front. If a large number of gripping sites fail and slip back, the cell's migration will become less efficient. In our model, higher level of myosin II triggers stronger gripping stress (Figure 5.4D), as has been observed in experiments [45, 97]. But it also pulls off more gripping sites (Figure 5.4E) and thus reduces cell speed when F^0_{grip} is high.

Similarly, we investigated how cell shape changes with myosin II and gripping strength (see Figure 5.5). The initial myosin II density is varied from $0.4\mu m^{-2}$ (top row), to $0.3\mu m^{-2}$ (middle row), and down to $0.2\mu m^{-2}$ (bottom row). The gripping strength is tuned by the parameter F^0_{grip}, which is assigned 1 Pa for the left column, 5 Pa for the middle column and 10 Pa for the right column. Note that all the cell shapes shown in the diagram are stationary except the one in the right-bottom corner, which keeps on oscillating. One feature in the cell shape is the aspect ratio, which is defined as the ratio between the width and the length of the cell. It measures how wide the cell is. When the gripping strength is low, which corresponds to the left column, the aspect ratio decreases as the amount of myosin II rises. This is due to the contracting effect of myosin II. As the gripping strength is increased from left to right, cells with different levels of myosin II behave differently. The cells with high level of myosin II (top row) become increasingly wider since the flanks of the cells are anchored by the gripping sites and are not easily pulled in by myosin contraction. However, the aspect ratio in the middle row does not change monotonically with gripping strength. After reaching a large aspect ratio of 2.6 in the middle frame, the cell becomes rounder when gripping strength further increases. In fact, when gripping strength gets too big, some adhesion sites stick to the substrate and do not turnover normally. Thus the aspect ratio decreases and cell migration is hindered. Cells in the bottom row have the lowest level of myosin II, and the gripping stress becomes very strong relative to myosin contraction. Consequently, the trailing part of the cell cannot peel off

the substrate efficiently. In sum, the overall diagram of cell shapes indicates that the shape of the cell is determined by the joint effect of myosin contraction and adhesion. This result is generally consistent with the experimental results [3], except that cells with lower myosin activity and higher adhesion strength have noisy periphery in experiment.

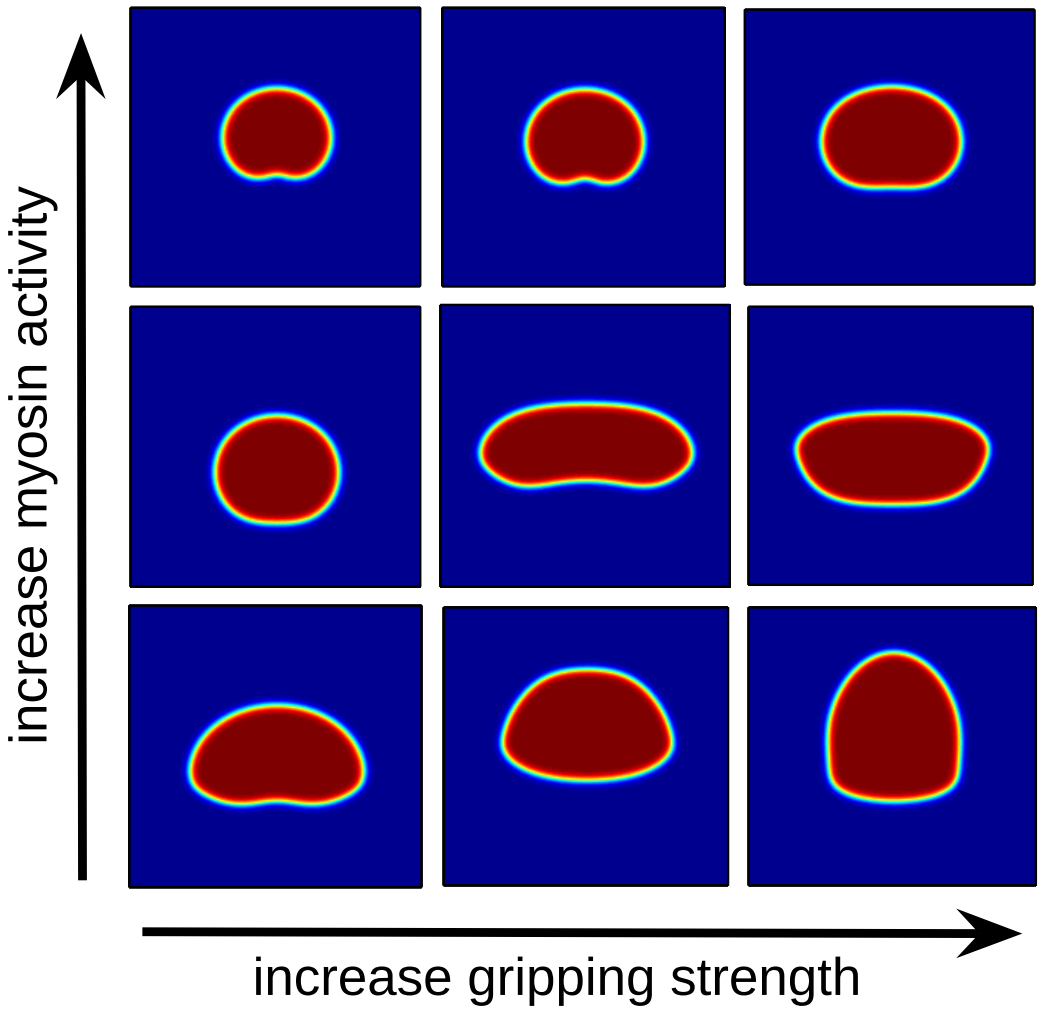

Figure 5.5: The phase diagram of cell shapes controlled by myosinII activity and gripping strength. The myosin activity is tuned by the initial concentration of myosin II: $[\rho_m^0] = 0.2\mu\text{m}^{-2}$ for bottom row, $[\rho_m^0] = 0.3\mu\text{m}^{-2}$ for middle row, and $[\rho_m^0] = 0.4\mu\text{m}^{-2}$ for top row; while the gripping strength is tuned by F_{grip}^0: $F_{grip}^0 = 1$Pa (left column), $F_{grip}^0 = 5$Pa (middle column) and $F_{grip}^0 = 10$Pa (right column).

5.4 Discussion

We built a comprehensive model on crawling keratocyte, which integrated actin polymerization, myosin contraction, adhesions and membrane forces. Many previous models [3, 99] treated actin polymerization as a protrusion speed v_p, and updated the cell shape by a phenomenal function of v_p. In contrary, we modeled it as an active stress [12]. In this way, the effect from actin polymerization and membrane tension can feed into the retrograde flow. Moreover, the cell boundary can evolve naturally by following the local actin flow velocity that result from various stresses.

Adhesion has long been modeled as a pure frictional drag, which cannot explain the alignment of the actin flow and substrate stress in the central part of the cell [31]. we incorporated the gripping mode into the adhesion mechanism and added dynamics for adhesion sites. Our model successfully produced the maps of actin flow, substrate stress and their alignment, and all the maps are in good agreement with experimental observation.

we further investigated how cell behaves under various levels of myosin II density and gripping strength. Simply put, the actin flow, cell velocity and the cell shape are controlled by the collective effect of myosin II and gripping strength rather by a single factor. Our model also suggested that there be an optimal level of myosin II and gripping strength for cell motility.

Myosin II mutants have been studied intensively and multiple roles have been proposed for myosin II. Aside from the well accepted function of contracting actin network, it might also strengthen the adhesion sites. For example, it was reported that cells treated with ML7 (a potent myosin II inhibitor) had less gelation traction force and less focal adhesions [45]. When myosin II is reduced in our model, although the gripping strength decreases, the number of gripping sites increases. If myosinII were indeed able to stabilize griping sites, we could improve our model by including that function, and the model predicted cell velocity would go higher relative to the current result for cells with reduced myosin II.

The reaction diffusion equations have changed from previous work [86] such that the cross linked actin network can polarize by its own. It agrees with the fact

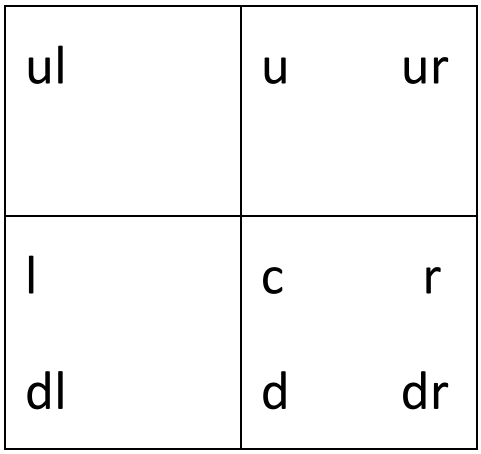

Figure 5.6: Illustration of computing space (c: center, l: left, r: right, u: up, d: down, ul: upper-left, ur: upper-right, dl: lower-left, dr: lower-right).

that myosin II mutants can remain polarized and move forward. Under the new model, we can study the effect of myosin II separately. However, the current model still has some limitations. It is sensible to the total amount of rho_a. If ρ_a^{tot} is outside a certain range, the cell can no longer polarize [68]. It's possible that there are extra pathways to control ρ_a^{tot}. Another possibility is that myosin II might dissemble F-actin near the cell back, as was suggested in [97].

This chapter is based on the following paper:

D. Shao, W.J. Rappel and H. Levine. Coupling actin flow and adhesion mechanism during cell migration. *In preparation.*

5.5 Appendix

5.5.1 Computational details

The partial differential equations are solved using finite difference method, which is much easier to implement than finite element method. In the two dimensional space, the grids are spaced Δx in the x direction and Δy in the y direction.

The actin flow equation

$$\upsilon_0 \nabla \cdot [\phi(\nabla \mathbf{u} + \nabla \mathbf{u}^T)] + \nabla \cdot \sigma_{\text{myo}} + \nabla \cdot \sigma_{\text{poly}} + \mathbf{F}_{\text{adh}} + \mathbf{F}_{\text{mem}} = \mathbf{0} \tag{5.1}$$

can be written as

$$\begin{aligned}
& \upsilon_0 \nabla \cdot [\phi(\nabla \mathbf{u} + \nabla \mathbf{u}^T)] \\
= \; & \upsilon_0 (\frac{\partial}{\partial x}, \frac{\partial}{\partial y}) \begin{pmatrix} 2\phi \frac{\partial u^x}{\partial x} & \phi \frac{\partial u^x}{\partial y} + \phi \frac{\partial u^y}{\partial x} \\ \phi \frac{\partial u^y}{\partial x} + \phi \frac{\partial u^x}{\partial y} & 2\phi \frac{\partial u^y}{\partial y} \end{pmatrix} \\
= \; & \upsilon_0 [2\frac{\partial}{\partial x}(\phi \frac{\partial u^x}{\partial x}) + \frac{\partial}{\partial y}(\phi \frac{\partial u^x}{\partial y}) + \frac{\partial}{\partial y}(\phi \frac{\partial u^y}{\partial x}), \\
& \frac{\partial}{\partial x}(\phi \frac{\partial u^y}{\partial x}) + 2\frac{\partial}{\partial y}(\phi \frac{\partial u^y}{\partial y}) + \frac{\partial}{\partial x}(\phi \frac{\partial u^x}{\partial y})]
\end{aligned}$$

Here u^x denotes the x-component of the actin flow velocity $\mathbf{u}$, while u^y denotes the y-component. We further use subscripts to label the positions relative to the central grid (see Figure 5.6). The above equation becomes: in the x direction

$$\begin{aligned}
& \frac{\upsilon_0}{\Delta x^2}[(\phi_l + \phi_c)u_l^x - (\phi_l + 2\phi_c + \phi_r)u_c^x + (\phi_c + \phi_r)u_r^x] \\
+ & \frac{\upsilon_0}{2\Delta y^2}[(\phi_u + \phi_c)u_u^x - (\phi_u + 2\phi_c + \phi_d)u_c^x + (\phi_c + \phi_d)u_d^x] \\
& + \frac{\upsilon_0}{4\Delta x \Delta y}[\phi_d(u_{dr}^y - u_{dl}^y) - \phi_u(u_{ur}^y - u_{ul}^y)],
\end{aligned}$$

and in the y direction

$$\begin{aligned}
& \frac{\upsilon_0}{2\Delta x^2}[(\phi_l + \phi_c)u_l^y - (\phi_l + 2\phi_c + \phi_r)u_c^y + (\phi_c + \phi_r)u_r^y] \\
+ & \frac{\upsilon_0}{\Delta y^2}[(\phi_u + \phi_c)u_u^y - (\phi_u + 2\phi_c + \phi_d)u_c^y + (\phi_c + \phi_d)u_d^y] \\
& + \frac{\upsilon_0}{4\Delta x \Delta y}[\phi_r(u_{dr}^x - u_{ur}^x) - \phi_l(u_{dl}^x - u_{ul}^y)]
\end{aligned}$$

Plug these into Eqn. 5.1, and write other terms in the similar way, we get

$$Ł_x^x u^x + L_y^x u^x + F_{eff}^x = 0 \tag{5.2}$$

$$Ł_x^y u^y + L_y^y u^y + F_{eff}^y = 0 \tag{5.3}$$

where L_x^x, L_y^x, L_x^y and L_y^y are the operators defined as

$$L_x^x = \begin{pmatrix} \frac{\upsilon_0}{\Delta x^2}(\phi_l + \phi_c) \\ -\frac{\upsilon_0}{\Delta x^2}(\phi_l + 2\phi_c + \phi_r) - \xi \\ \frac{\upsilon_0}{\Delta x^2}(\phi_c + \phi_r) \end{pmatrix}$$

$$L_y^x = \begin{pmatrix} \frac{\upsilon_0}{2\Delta y^2}(\phi_u + \phi_c) \\ -\frac{\upsilon_0}{2\Delta y^2}(\phi_u + 2\phi_c + \phi_d) \\ \frac{\upsilon_0}{2\Delta y^2}(\phi_c + \phi_d) \end{pmatrix}$$

$$L_x^y = \begin{pmatrix} \frac{\upsilon_0}{2\Delta x^2}(\phi_l + \phi_c) \\ -\frac{\upsilon_0}{2\Delta x^2}(\phi_l + 2\phi_c + \phi_r) - \xi \\ \frac{\upsilon_0}{2\Delta x^2}(\phi_c + \phi_r) \end{pmatrix}$$

$$L_y^y = \begin{pmatrix} \frac{\upsilon_0}{\Delta y^2}(\phi_u + \phi_c) \\ -\frac{\upsilon_0}{\Delta y^2}(\phi_u + 2\phi_c + \phi_d) \\ \frac{\upsilon_0}{\Delta y^2}(\phi_c + \phi_d) \end{pmatrix}$$

and

$$F_{eff}^x = \frac{\upsilon_0}{4\Delta x \Delta y}[\phi_r(u_{dr}^y - u_{ur}^y) - \phi_l(u_{dl}^y - u_{ul}^y)] + F^x$$

$$F_{eff}^y = \frac{\upsilon_0}{4\Delta x \Delta y}[\phi_r(u_{dr}^x - u_{ur}^x) - \phi_l(u_{dl}^x - u_{ul}^x)] + F^y$$

Here F^x and F^y include the myosin II contraction, F-actin protrusion, and the forces from the adhesion sites.

We use relaxation method to solve Eqn. 5.2 and Eqn. 5.3. That is, we solve

$$\frac{\partial u}{\partial t} = Ł_x u + L_y u + F_{eff} \tag{5.4}$$

for multiple iterations until we reach a steady state.

Eqn. 5.4 has operators in both x and y directions, and thus we use ADI (Alternating Directional Implicit Method) method. We separate it into two steps and solve one operator in each step. Specifically, Eqn. 5.4 can be implemented in the Crank-Nicolson scheme

$$\frac{u^{n+1} - u^n}{\Delta t} = (L_x + L_y)\frac{u^n + u^{n+1}}{2} + F_{eff}$$

Let $v = u^{n+1} - u^n$, then

$$(\frac{I}{\Delta t} - \frac{1}{2}L_x - \frac{1}{2}L_y)v = (L_x + L_y)u^n + F_{eff}.$$

When Δt is small,

$$I - \frac{1}{2}\Delta t L_x - \frac{1}{2}\Delta t L_y \sim (I - \frac{1}{2}\Delta t L_x)(I - \frac{1}{2}\Delta t L_y)$$

We get

$$\begin{aligned}(I - \frac{1}{2}\Delta t L_x)w &= [(L_x + L_y)u + F_{eff}]\Delta t \\ (I - \frac{1}{2}\Delta t L_y)v &= w\end{aligned}$$

Let $\eta = \frac{2}{\Delta t}$, then

$$(L_x - \eta)w = -2[(L_x + L_y)u + F_{eff}]\Delta t \tag{5.5}$$

$$(L_y - \eta)v = -\eta w \tag{5.6}$$

Eqn. 5.5 and Eqn. 5.6 can be easily solved by LU decomposition. Then we update u^n to u^{n+1} using $u^{n+1} = u^n + v$ for each iteration.

Reaction-diffusion equations and the evolution equation for the phase-field are solved using explicit method.

Chapter 6

Closing remarks

Cell migration is very complex. It consists of several modules, including signaling pathways, actin polymerization, myosin contraction and adhesion. It can also be modeled on different scales, for example, molecular scale, cellular scale, or in between.

In Chapter 2, we studied the Ras adaptation under a uniform stimulus. Although we got good response curves up to 35 seconds, the model did not capture the response afterwards. In the experiment, a second peak was observed consistently, which was probably due to the downstream feedback. In fact, there are many other components in the signaling pathway where Ras resides. Above Ras, there is G protein, which can activates multiple pathways. Downstream from Ras are PI3K, PIP3, actin, etc. Moreover, the possible feedbacks between Ras, PI3K, PIP3 and actin, along with the crosstalks with other signaling pathways complicate the problem [15]. Therefore, One future direction is to gradually include those components and get a better understanding of the overall picture.

One important function of the Ras pathway is to sense the external gradient. In fact, Dictyostelium cells are able to sense a gradient as shallow as 5 percent. Moreover, it has been observed that Ras can amplify the external gradient dramatically, which is not predicted by the vanilla model presented in Chapter 2. There must be some extra mechanism to amplify the gradient, such as the ultra-sensitivity mechanism. Future models can incorporate and test those mechanisms.

From Chapter 3 to Chapter 5, we built a framework that integrated chemical

reactions, actomyosin mechanical engine and adhesions together based on the phase field method. The phase field method is very powerful in solving moving boundary problems, and has been successfully applied to vesicles. However, its potential was not fully realized in the cell migration study. To build a framework based on the phase field method, we cleared several obstacles out. For example, the boundary conditions for a moving and deforming cell, including no flux of chemicals across the boundary and zero net stress. Also the profile of the interface was maintained consistently. Under this frame work, we managed to develop comprehensive models on keratocytes and Dictyostelium cells.

Most previous models treated the adhesion mechanism as purely frictional drag. In our model, the adhesion sites were either in the gripping mode (spring-like force) or in the slipping mode (frictional drag). Our model was able to explain the nonalignment in the central part of the cell, which was consistent with the experimental observations. However, the detailed regulations on adhesion dynamics need further clarification. For example, how the adhesion sites are regulated by chemical signaling pathways, how they interact with the actin network, their maturation process, and how the force is generated. Also, the substrate properties, such as rigidity, may also affect the effectiveness of cell migration, providing another interesting topic.

The reaction diffusion equations were changed from Chapter 4 to Chapter 5. In the model of Chapter 4, the symmetry breaking was driven by myosin. Once the cell started moving in a certain direction, myosin was left behind and generated retraction forces. The distribution of F-actin was then determined by myosin. If myosin were deleted from the system, the cell would lose its motility. However, experiments have shown that mutants with myosin inhibited can still move, indicating that F-actin has its own symmetry breaking mechanism. The model in Chapter 5 was designed based on this conclusion. In this model, the total amount of actin was conserved. Moreover, the ratio between the total amount of actin and the cell area needs to fall in an intermediate range such that certain percentage of actin was in the active state while the rest in the inactive state. However, since the cell area may change during the migration, the actin/area ratio

may change accordingly and slip out of the required range, and the cell will lose its asymmetry. It's possible that there exists some extra mechanism to control the total area of the cell. Otherwise the cell needs some other symmetry breaking mechanism. Given the complexity of the system, it's very likely that cells employ more than one regulatory mechanisms.

We had a hard time to get a stationary fan-like shape for keratocytes, especially those with large aspect ratios. Actually, the model employing Chapter 4's reaction-diffusion equations cannot give an aspect ratio larger than 1.8. The accumulated myosin at the back of the cell tend to concave the membrane nearby. Once the cell gets wider, myosin can easily diffuse into the front of cell and concave the membrane along the leading edge, causing the cell to divide. Though this is not the desired behavior in cell migration, it may be used to model mitosis in eukaryotes and binary fission in prokaryotes.

There have been conflicting reports on the behavior of myosin mutants [3, 31, 45, 103, 97]. Our model predicted that the cell shape, cell speed and actin flow were determined by the interaction of myosin and adhesion. Further collaboration between modeling and experimental studies will foster a better understanding on this topic.

In Chapter 4, we built a minimal model for Dictyostelium. That model had a single patch and the patch's birthplace distribution followed a simple delta function. In the more realistic model [39], Hecht *et al.* used a couple of reaction diffusion equations to regulate the patch signaling and modeled the phenomenon of splitting of pseudopods. However, their model was defined only along the 1D membrane. A future model combining the power of the phase field framework and the biological details would help to unravel the mechanisms underlying the chemotaxis of Dictyostelium cells.

Bibliography

[1] K. I. Anderson and R. Cross. Contact dynamics during keratocyte motility. *Curr. Biol.*, 10:253–260, Mar 2000.

[2] N. Barkai and S. Leibler. Robustness in simple biochemical networks. *Nature*, 387:913–917, Jun 1997.

[3] E. L. Barnhart, K. C. Lee, K. Keren, A. Mogilner, and J. A. Theriot. An adhesion-dependent switch between mechanisms that determine motile cell shape. *PLoS Biol.*, 9:e1001059, 2011.

[4] M. Behar, N. Hao, H. G. Dohlman, and T. C. Elston. Mathematical and computational analysis of adaptation via feedback inhibition in signal transduction pathways. *Biophys. J.*, 93:806–821, Aug 2007.

[5] K. A. Beningo, M. Dembo, I. Kaverina, J. V. Small, and Y. L. Wang. Nascent focal adhesions are responsible for the generation of strong propulsive forces in migrating fibroblasts. *J. Cell Biol.*, 153:881–888, 2001.

[6] H. C. Berg and D. A. Brown. Chemotaxis in Escherichia coli analysed by three-dimensional tracking. *Nature*, 239:500–504, Oct 1972.

[7] C. Beta, G. Amselem, and E. Bodenschatz. A bistable mechanism for directional sensing. *New Journal of Physics*, 10:083015, Aug 2008.

[8] T. Biben, K. Kassner, and C. Misbah. Phase-field approach to three-dimensional vesicle dynamics. *Phys Rev E Stat Nonlin Soft Matter Phys*, 72:041921, Oct 2005.

[9] T. Biben and C. Misbah. Tumbling of vesicles under shear flow within an advected-field approach. *Phys. Rev. E*, 67(3):031908, Mar 2003.

[10] M. Buenemann, H. Levine, W. J. Rappel, and L. M. Sander. The role of cell contraction and adhesion in dictyostelium motility. *Biophys. J.*, 99:50–58, 2010.

[11] F. Campelo and F. Hernandez-machado. Dynamic model and stationary shapes of fluid vesicles. *Eur. Phys. J. E*, 20:37–45, 2006.

[12] A. E. Carlsson. Mechanisms of cell propulsion by active stresses. *New J. Phys.*, 13:073009, 2011.

[13] C. E. Chan and D. J. Odde. Traction dynamics of filopodia on compliant substrates. *Science*, 322:1687–1691, Dec 2008.

[14] P. G. Charest and R. A. Firtel. Feedback signaling controls leading-edge formation during chemotaxis. *Curr. Opin. Genet. Dev.*, 16:339–347, Aug 2006.

[15] P. G. Charest, Z. Shen, A. Lakoduk, A. T. Sasaki, S. P. Briggs, and R. A. Firtel. A Ras signaling complex controls the RasC-TORC2 pathway and directed cell migration. *Dev. Cell*, 18:737–749, May 2010.

[16] C. K. Choi, M. Vicente-Manzanares, J. Zareno, L. A. Whitmore, A. Mogilner, and A. R. Horwitz. Actin and alpha-actinin orchestrate the assembly and maturation of nascent adhesions in a myosin II motor-independent manner. *Nat. Cell Biol.*, 10:1039–1050, 2008.

[17] M. Cirit, M. Krajcovic, C. K. Choi, E. S. Welf, A. F. Horwitz, and J. M. Haugh. Stochastic model of integrin-mediated signaling and adhesion dynamics at the leading edges of migrating cells. *PLoS Comput. Biol.*, 6:e1000688, 2010.

[18] L. P. Cramer. Molecular mechanism of actin-dependent retrograde flow in lamellipodia of motile cells. *Front. Biosci*, 2:d260–270, 1997.

[19] J. Dai, H. P. Ting-Beall, R. M. Hochmuth, M. P. Sheetz, and M. A. Titus. Myosin I contributes to the generation of resting cortical tension. *Biophys. J.*, 77:1168–1176, Aug 1999.

[20] J. Das, M. Ho, J. Zikherman, C. Govern, M. Yang, A. Weiss, A. K. Chakraborty, and J. P. Roose. Digital signaling and hysteresis characterize ras activation in lymphoid cells. *Cell*, 136:337–351, Jan 2009.

[21] J. C. Del Alamo, R. Meili, B. Alonso-Latorre, J. Rodriguez-Rodriguez, A. Aliseda, R. A. Firtel, and J. C. Lasheras. Spatio-temporal analysis of eukaryotic cell motility by improved force cytometry. *Proc. Natl. Acad. Sci. U.S.A.*, 104:13343–13348, Aug 2007.

[22] M. Dembo and F. Harlow. Cell motion, contractile networks, and the physics of interpenetrating reactive flow. *Biophys. J.*, 50:109–121, Jul 1986.

[23] R. B. Dickinson. Models for actin polymerization motors. *J Math Biol*, 58:81–103, Jan 2009.

[24] Qiang Du, Chun Liu, and Xiaoqiang Wang. Simulating the deformation of vesicle membranes under elastic bending energy in three dimensions. *J. Comput. Phys.*, 212(2):757–777, 2006.

[25] H. El-Samad, J. P. Goff, and M. Khammash. Calcium homeostasis and parturient hypocalcemia: an integral feedback perspective. *J. Theor. Biol.*, 214:17–29, Jan 2002.

[26] R. G. Endres and N. S. Wingreen. Precise adaptation in bacterial chemotaxis through "assistance neighborhoods". *Proc. Natl. Acad. Sci. U.S.A.*, 103:13040–13044, Aug 2006.

[27] U. Euteneuer and M. Schliwa. Persistent, directional motility of cells and cytoplasmic fragments in the absence of microtubules. *Nature*, 310:58–61, 1984.

[28] F. H. Fenton, E. M. Cherry, A. Karma, and W. J. Rappel. Modeling wave propagation in realistic heart geometries using the phase-field method. *Chaos*, 15:13502, Mar 2005.

[29] M. Fivaz, S. Bandara, T. Inoue, and T. Meyer. Robust neuronal symmetry breaking by Ras-triggered local positive feedback. *Curr. Biol.*, 18:44–50, Jan 2008.

[30] R. Folch, J. Casademunt, A. Hernandez-Machado, and L. Ramirez-Piscina. Phase-field model for Hele-Shaw flows with arbitrary viscosity contrast. I. Theoretical approach. *Phys Rev E Stat Phys Plasmas Fluids Relat Interdiscip Topics*, 60:1724–1733, Aug 1999.

[31] M. F. Fournier, R. Sauser, D. Ambrosi, J. J. Meister, and A. B. Verkhovsky. Force transmission in migrating cells. *J. Cell Biol.*, 188:287–297, Jan 2010.

[32] D. Fuller, W. Chen, M. Adler, A. Groisman, H. Levine, W. J. Rappel, and W. F. Loomis. External and internal constraints on eukaryotic chemotaxis. *Proc. Natl. Acad. Sci. U.S.A.*, 107:9656–9659, May 2010.

[33] S. Funamoto, R. Meili, S. Lee, L. Parry, and R. A. Firtel. Spatial and temporal regulation of 3-phosphoinositides by PI 3-kinase and PTEN mediates chemotaxis. *Cell*, 109:611–623, May 2002.

[34] M. L. Gardel, I. C. Schneider, Y. Aratyn-Schaus, and C. M. Waterman. Mechanical integration of actin and adhesion dynamics in cell migration. *Annu. Rev. Cell Dev. Biol.*, 26:315–333, 2010.

[35] B. Geiger and K. M. Yamada. Molecular architecture and function of matrix adhesions. *Cold Spring Harb Perspect Biol*, 3, May 2011.

[36] A. Goldbeter and D. E. Koshland. An amplified sensitivity arising from covalent modification in biological systems. *Proc. Natl. Acad. Sci. U.S.A.*, 78:6840–6844, Nov 1981.

[37] M. E. Gracheva and H. G. Othmer. A continuum model of motility in ameboid cells. *Bull. Math. Biol.*, 66:167–193, Jan 2004.

[38] I. Hecht, D. A. Kessler, and H. Levine. Transient localized patterns in noise-driven reaction-diffusion systems. *Phys. Rev. Lett.*, 104:158301, Apr 2010.

[39] Charest PG Ben-Jacob E Firtel RA Loomis WF Levine H Rappel WJ. Hecht I, Skoge ML. Activated membrane patches guide chemotactic cell motility. *PLoS Comput Biol.*, 7(6):e1002044, 2011.

[40] W. Helfrich. Elastic properties of lipid bilayerstheory and possible experiments. *Z. Naturforsch. C*, 28:693–703, 1973.

[41] M. Herant and M. Dembo. Form and function in cell motility: from fibroblasts to keratocytes. *Biophys. J.*, 98:1408–1417, Apr 2010.

[42] C. Janetopoulos and R. A. Firtel. Directional sensing during chemotaxis. *FEBS Lett.*, 582:2075–2085, Jun 2008.

[43] C. Janetopoulos, T. Jin, and P. Devreotes. Receptor-mediated activation of heterotrimeric G-proteins in living cells. *Science*, 291:2408–2411, Mar 2001.

[44] B. M. Jockusch, P. Bubeck, K. Giehl, M. Kroemker, J. Moschner, M. Rothkegel, M. Rudiger, K. Schluter, G. Stanke, and J. Winkler. The molecular architecture of focal adhesions. *Annu. Rev. Cell Dev. Biol.*, 11:379–416, 1995.

[45] C. Jurado, J. R. Haserick, and J. Lee. Slipping or gripping? Fluorescent speckle microscopy in fish keratocytes reveals two different mechanisms for generating a retrograde flow of actin. *Mol. Biol. Cell*, 16:507–518, Feb 2005.

[46] H. Kae, A. Kortholt, H. Rehmann, R. H. Insall, P. J. Van Haastert, G. B. Spiegelman, and G. Weeks. Cyclic AMP signalling in Dictyostelium: G-proteins activate separate Ras pathways using specific RasGEFs. *EMBO Rep.*, 8:477–482, May 2007.

[47] A. Karma, D. A. Kessler, and H. Levine. Phase-field model of mode III dynamic fracture. *Phys. Rev. Lett.*, 87:045501, Jul 2001.

[48] K. Keren, Z. Pincus, G. M. Allen, E. L. Barnhart, G. Marriott, A. Mogilner, and J. A. Theriot. Mechanism of shape determination in motile cells. *Nature*, 453:475–480, May 2008.

[49] J. Kockelkoren, H. Levine, and W. J. Rappel. Computational approach for modeling intra- and extracellular dynamics. *Phys Rev E Stat Nonlin Soft Matter Phys*, 68:037702, Sep 2003.

[50] B. Kutscher, P. Devreotes, and P. A. Iglesias. Local excitation, global inhibition mechanism for gradient sensing: an interactive applet. *Sci. STKE*, 2004:pl3, Feb 2004.

[51] K. Larripa and A. Mogilner. Transport of a 1D viscoelastic actin-myosin strip of gel as a model of a crawling cell. *Physica A*, 372:113–123, Dec 2006.

[52] T. Lecuit and P. F. Lenne. Cell surface mechanics and the control of cell shape, tissue patterns and morphogenesis. *Nat. Rev. Mol. Cell Biol.*, 8:633–644, Aug 2007.

[53] J. Lee, A. Ishihara, J. A. Theriot, and K. Jacobson. Principles of locomotion for simple-shaped cells. *Nature*, 362:167–171, Mar 1993.

[54] A. Levchenko and P. A. Iglesias. Models of eukaryotic gradient sensing: application to chemotaxis of amoebae and neutrophils. *Biophys. J.*, 82:50–63, Jan 2002.

[55] H. Levine, D. A. Kessler, and W. J. Rappel. Directional sensing in eukaryotic chemotaxis: a balanced inactivation model. *Proc. Natl. Acad. Sci. U.S.A.*, 103:9761–9766, Jun 2006.

[56] J. S. Lowengrub, A. Ratz, and A. Voigt. Phase-field modeling of the dynamics of multicomponent vesicles: Spinodal decomposition, coarsening, budding, and fission. *Phys Rev E Stat Nonlin Soft Matter Phys*, 79:031926, Mar 2009.

[57] J. S. Lowengrub, A. Ratz, and A. Voigt. Phase-field modeling of the dynamics of multicomponent vesicles: Spinodal decomposition, coarsening, budding, and fission. *Phys Rev E Stat Nonlin Soft Matter Phys*, 79:031926, Mar 2009.

[58] W. Ma, A. Trusina, H. El-Samad, W. A. Lim, and C. Tang. Defining network topologies that can achieve biochemical adaptation. *Cell*, 138:760–773, Aug 2009.

[59] A. F. Maree, A. Jilkine, A. Dawes, V. A. Grieneisen, and L. Edelstein-Keshet. Polarization and movement of keratocytes: a multiscale modelling approach. *Bull. Math. Biol.*, 68:1169–1211, Jul 2006.

[60] R. Meili, C. Ellsworth, S. Lee, T. B. Reddy, H. Ma, and R. A. Firtel. Chemoattractant-mediated transient activation and membrane localization of Akt/PKB is required for efficient chemotaxis to cAMP in Dictyostelium. *EMBO J.*, 18:2092–2105, Apr 1999.

[61] R. Merkel, R. Simson, D. A. Simson, M. Hohenadl, A. Boulbitch, E. Wallraff, and E. Sackmann. A micromechanic study of cell polarity and plasma membrane cell body coupling in Dictyostelium. *Biophys. J.*, 79:707–719, Aug 2000.

[62] G. L. Ming, S. T. Wong, J. Henley, X. B. Yuan, H. J. Song, N. C. Spitzer, and M. M. Poo. Adaptation in the chemotactic guidance of nerve growth cones. *Nature*, 417:411–418, May 2002.

[63] A. Mogilner. Mathematics of cell motility: have we got its number? *J Math Biol*, 58:105–134, Jan 2009.

[64] A. Mogilner and K. Keren. The shape of motile cells. *Curr. Biol.*, 19:R762–771, Sep 2009.

[65] A. Mogilner and G. Oster. Polymer motors: pushing out the front and pulling up the back. *Curr. Biol.*, 13:R721–733, Sep 2003.

[66] Y. Mori, A. Jilkine, and L. Edelstein-Keshet. Wave-pinning and cell polarity from a bistable reaction-diffusion system. *Biophys. J.*, 94:3684–3697, May 2008.

[67] D. Muzzey, C. A. Gomez-Uribe, J. T. Mettetal, and A. van Oudenaarden. A systems-level analysis of perfect adaptation in yeast osmoregulation. *Cell*, 138:160–171, Jul 2009.

[68] M. Otsuji, S. Ishihara, C. Co, K. Kaibuchi, A. Mochizuki, and S. Kuroda. A mass conserved reaction-diffusion system captures properties of cell polarity. *PLoS Comput. Biol.*, 3:e108, Jun 2007.

[69] C. A. Parent, B. J. Blacklock, W. M. Froehlich, D. B. Murphy, and P. N. Devreotes. G protein signaling events are activated at the leading edge of chemotactic cells. *Cell*, 95:81–91, Oct 1998.

[70] C. A. Parent and P. N. Devreotes. A cell's sense of direction. *Science*, 284:765–770, Apr 1999.

[71] K. C. Park, F. Rivero, R. Meili, S. Lee, F. Apone, and R. A. Firtel. Rac regulation of chemotaxis and morphogenesis in Dictyostelium. *EMBO J.*, 23:4177–4189, Oct 2004.

[72] T. D. Pollard and G. G. Borisy. Cellular motility driven by assembly and disassembly of actin filaments. *Cell*, 112:453–465, Feb 2003.

[73] M. Postma and P. J. Van Haastert. A diffusion-translocation model for gradient sensing by chemotactic cells. *Biophys. J.*, 81:1314–1323, Sep 2001.

[74] W. H. Press, S. A. Teukolsky, W. T. Vetterling, and B. P. Flannery. *Numerical Recipes: The Art of Scientific Computing*. Cambridge University Press, 3rd edition, 2007.

[75] W. J. Rappel. Filament instability and rotational tissue anisotropy: A numerical study using detailed cardiac models. *Chaos*, 11:71–80, Mar 2001.

[76] W. J. Rappel and W. F. Loomis. Eukaryotic chemotaxis. *Wiley Interdiscip Rev Syst Biol Med*, 1:141–149, 2009.

[77] W. J. Rappel, P. J. Thomas, H. Levine, and W. F. Loomis. Establishing direction during chemotaxis in eukaryotic cells. *Biophys. J.*, 83:1361–1367, Sep 2002.

[78] E. M. Reichl, Y. Ren, M. K. Morphew, M. Delannoy, J. C. Effler, K. D. Girard, S. Divi, P. A. Iglesias, S. C. Kuo, and D. N. Robinson. Interactions between myosin and actin crosslinkers control cytokinesis contractility dynamics and mechanics. *Curr. Biol.*, 18:471–480, Apr 2008.

[79] B. Rubinstein, M. F. Fournier, K. Jacobson, A. B. Verkhovsky, and A. Mogilner. Actin-myosin viscoelastic flow in the keratocyte lamellipod. *Biophys. J.*, 97:1853–1863, Oct 2009.

[80] A. T. Sasaki, C. Chun, K. Takeda, and R. A. Firtel. Localized Ras signaling at the leading edge regulates PI3K, cell polarity, and directional cell movement. *J. Cell Biol.*, 167:505–518, Nov 2004.

[81] A. T. Sasaki, C. Janetopoulos, S. Lee, P. G. Charest, K. Takeda, L. W. Sundheimer, R. Meili, P. N. Devreotes, and R. A. Firtel. G protein-independent Ras/PI3K/F-actin circuit regulates basic cell motility. *J. Cell Biol.*, 178:185–191, Jul 2007.

[82] J. Satulovsky, R. Lui, and Y. L. Wang. Exploring the control circuit of cell migration by mathematical modeling. *Biophys. J.*, 94:3671–3683, May 2008.

[83] S. V. Satyanarayana and A. Baumgaertner. Shape and motility of a model cell: a computational study. *J Chem Phys*, 121:4255–4265, Sep 2004.

[84] S. Schaub, S. Bohnet, V. M. Laurent, J. J. Meister, and A. B. Verkhovsky. Comparative maps of motion and assembly of filamentous actin and myosin II in migrating cells. *Mol. Biol. Cell*, 18:3723–3732, Oct 2007.

[85] U. Seifert. Configurations of fluid membranes and vesicles. *Advances in Physics*, 46:13–137, 1997.

[86] D. Shao, W. J. Rappel, and H. Levine. Computational model for cell morphodynamics. *Phys. Rev. Lett.*, 105:108104, 2010.

[87] S. S. Shen-Orr, R. Milo, S. Mangan, and U. Alon. Network motifs in the transcriptional regulation network of Escherichia coli. *Nat. Genet.*, 31:64–68, May 2002.

[88] R. Simson, E. Wallraff, J. Faix, J. Niewohner, G. Gerisch, and E. Sackmann. Membrane bending modulus and adhesion energy of wild-type and mutant cells of Dictyostelium lacking talin or cortexillins. *Biophys. J.*, 74:514–522, Jan 1998.

[89] L. Song, S. M. Nadkarni, H. U. Bodeker, C. Beta, A. Bae, C. Franck, W. J. Rappel, W. F. Loomis, and E. Bodenschatz. Dictyostelium discoideum chemotaxis: threshold for directed motion. *Eur. J. Cell Biol.*, 85:981–989, Sep 2006.

[90] K. F. Swaney, C. H. Huang, and P. N. Devreotes. Eukaryotic chemotaxis: a network of signaling pathways controls motility, directional sensing, and polarity. *Annu Rev Biophys*, 39:265–289, Jun 2010.

[91] M. Ueda, Y. Sako, T. Tanaka, P. Devreotes, and T. Yanagida. Single-molecule analysis of chemotactic signaling in Dictyostelium cells. *Science*, 294:864–867, Oct 2001.

[92] P. Vallotton, G. Danuser, S. Bohnet, J. J. Meister, and A. B. Verkhovsky. Tracking retrograde flow in keratocytes: news from the front. *Mol. Biol. Cell*, 16:1223–1231, Mar 2005.

[93] P. J. Van Haastert and R. J. De Wit. Demonstration of receptor heterogeneity and affinity modulation by nonequilibrium binding experiments. The cell surface cAMP receptor of Dictyostelium discoideum. *J. Biol. Chem.*, 259:13321–13328, Nov 1984.

[94] P. J. Van Haastert and P. R. Van der Heijden. Excitation, adaptation, and deadaptation of the cAMP-mediated cGMP response in Dictyostelium discoideum. *J. Cell Biol.*, 96:347–353, Feb 1983.

[95] A. B. Verkhovsky, T. M. Svitkina, and G. G. Borisy. Self-polarization and directional motility of cytoplasm. *Curr. Biol.*, 9:11–20, Jan 1999.

[96] A. B. Verkhovsky, T. M. Svitkina, and G. G. Borisy. Self-polarization and directional motility of cytoplasm. *Curr. Biol.*, 9:11–20, Jan 1999.

[97] C. A. Wilson, M. A. Tsuchida, G. M. Allen, E. L. Barnhart, K. T. Applegate, P. T. Yam, L. Ji, K. Keren, G. Danuser, and J. A. Theriot. Myosin II contributes to cell-scale actin network treadmilling through network disassembly. *Nature*, 465:373–377, May 2010.

[98] T. P. Witelski and M. Bowen. Adi schemes for higher-order nonlinear diffusion equations. *Applied Numerical Mathematics*, 45:331 351, 2003.

[99] C. W. Wolgemuth, J. Stajic, and A. Mogilner. Redundant mechanisms for stable cell locomotion revealed by minimal models. *Biophys. J.*, 101:545–553, 2011.

[100] Y. Xiong, C. H. Huang, P. A. Iglesias, and P. N. Devreotes. Cells navigate with a local-excitation, global-inhibition-biased excitable network. *Proc. Natl. Acad. Sci. U.S.A.*, 107:17079–17086, Oct 2010.

[101] X. Xu, M. Meier-Schellersheim, X. Jiao, L. E. Nelson, and T. Jin. Quantitative imaging of single live cells reveals spatiotemporal dynamics of multistep signaling events of chemoattractant gradient sensing in Dictyostelium. *Mol. Biol. Cell*, 16:676–688, Feb 2005.

[102] X. Xu, M. Meier-Schellersheim, J. Yan, and T. Jin. Locally controlled inhibitory mechanisms are involved in eukaryotic GPCR-mediated chemosensing. *J. Cell Biol.*, 178:141–153, Jul 2007.

[103] P. T. Yam, C. A. Wilson, L. Ji, B. Hebert, E. L. Barnhart, N. A. Dye, P. W. Wiseman, G. Danuser, and J. A. Theriot. Actin-myosin network reorganization breaks symmetry at the cell rear to spontaneously initiate polarized cell motility. *J. Cell Biol.*, 178:1207–1221, Sep 2007.

[104] L. Yang, J. C. Effler, B. L. Kutscher, S. E. Sullivan, D. N. Robinson, and P. A. Iglesias. Modeling cellular deformations using the level set formalism. *BMC Syst Biol*, 2:68, 2008.

[105] L. Yang, J. C. Effler, B. L. Kutscher, S. E. Sullivan, D. N. Robinson, and P. A. Iglesias. Modeling cellular deformations using the level set formalism. *BMC Syst Biol*, 2:68, 2008.

[106] T. M. Yi, Y. Huang, M. I. Simon, and J. Doyle. Robust perfect adaptation in bacterial chemotaxis through integral feedback control. *Proc. Natl. Acad. Sci. U.S.A.*, 97:4649–4653, Apr 2000.

[107] Jian Zhang, Sovan Das, and Qiang Du. A phase field model for vesicle-substrate adhesion. *J. Comput. Phys.*, 228(20):7837–7849, 2009.

[108] S. Zhang, P. G. Charest, and R. A. Firtel. Spatiotemporal regulation of Ras activity provides directional sensing. *Curr. Biol.*, 18:1587–1593, Oct 2008.

[109] W. Zhang and D. N. Robinson. Balance of actively generated contractile and resistive forces controls cytokinesis dynamics. *Proc. Natl. Acad. Sci. U.S.A.*, 102:7186–7191, May 2005.

[110] S. H. Zigmond and S. J. Sullivan. Sensory adaptation of leukocytes to chemotactic peptides. *J. Cell Biol.*, 82:517–527, Aug 1979.

[111] J. Zimmermann, M. Enculescu, and M. Falcke. Leading-edge-gel coupling in lamellipodium motion. *Phys. Rev. E Stat. Nonlin. Soft. Matter Phys.*, 82:051925, 2010.